Research article

PG
Petroleum Geoscience

https://doi.org/10.1144/petgeo2023-009 | Vol. 29 | 2023 | petgeo2023-009

Gravity imaging of sub-Zechstein geological structures in the UK sector of the North Sea using the gravity layer stripping method

J. D. Fairhead[1,2*], D. Marsden[1], N. M. Azli[2], İ. Özsöz[2], D. Maxwell[2], O. Rose[2] and C. M. Green[2]

[1] Painted Wolf Resources Ltd., Chiswick, London, UK
[2] School of Earth and Environment, University of Leeds, Leeds, UK
JDF, 0000-0001-7610-324X
* Correspondence: jamesderekfairhead@gmail.com

Abstract: Extensive geophysical databases, covering the UK sector of the North Sea, have been used to gravity layer strip the sedimentary layers down to the base Zechstein so that the gravity response of the Carboniferous and deeper strata can be identified and structurally interpreted. To achieve this, the average bulk density grids for each layer were derived using Gardner's functions derived from well velocity and density logs. The resulting residual gravity response of each layer and the Moho response were then removed from the Free air gravity anomaly to generate the isostatic gravity response of the crust below the base Zechstein. This gravity response was used to re-evaluate the British Geological Survey interpretation over the Mid North Sea High (MNSH) and was able to identify the same crustal structures. Using the tilt derivative method, a positive gravity anomaly was found to parallel the central fracture zone that forms a northern extension of the Dowsing fault zone. This anomaly can be traced north across the MNSH with offsets coinciding with the WSW–ENE basement lineaments. To the south, the southern North Sea basin is well defined by the stratigraphic layer depth and thickness maps as well as the residual gravity maps which identify the structures associated with the low-density Carboniferous Coal Measures.

Received 26 January 2023; **revised** 1 August 2023; **accepted** 1 September 2023

The aim of this study is to investigate the sub-Zechstein geology and structure of the UK sector of the North Sea using the extensive geophysical and geological database compiled by the UK North Sea Transition Authority. To do this, the gravity response of the sedimentary layers down to the base Zechstein salt have been calculated and removed from the satellite derived Free air gravity leaving a residual gravity field that only contains sub-Zechstein and deeper tectonic, basement and sedimentary structures. This methodology is known as gravity layer stripping. In particular, the study wished to define the low-density concealed Upper Paleozoic basins, such as the Carboniferous basin structures beneath the Permian, Mesozoic and Cenozoic sediments, residing in the southern North Sea (SNS) and represent the UK's largest gas producing basin.

The geological setting of the UK sector of the North Sea is that it covers the western part of a major subsiding rift system, whose axis extends regionally from south to north as the Lower Rhine Graben, the Central Graben and the Viking Graben. This is illustrated in a summary geological map (Fig. 1) where the blue area defines the main upper Jurassic depositional centres associated with this rift system.

Geological studies indicate that multiple rift phases occurred in the late Paleozoic and early Mesozoic which allowed the opening of the northeastern Atlantic. During this period, the North Sea rifting failed to reach an oceanic crustal stage of development. The initial stage of rifting is considered to have commenced at approximately the start of the Variscan Orogeny (380 Ma) and ended in the Permian. The Late Permian deposition of evaporites created the Zechstein supergroup which acted as a salt cap rock to the fine-grained sediment beneath trapping the gas sourced from the Carboniferous Westphalian and Namurian strata. Further active crustal stretching, thinning and rifting occurred in the Triassic, Jurassic and Cretaceous resulting in isostatic subsidence and sedimentation. During the Cenozoic (referred to as Tertiary in the text) a broad synclinal sag basin developed, centred over the rift system, with subsidence more intense over the eastern half of the UK sector. This subsidence is due to the upper mantle cooling and thermally contracting.

The UK section of the North Sea, particularly the SNS, is a mature exploration province for gas and is now covered and penetrated by an extensive set of 2D and 3D seismic reflection surveys and well data respectively (Fig. 2). These data are, in the main, available from the North Sea Transition Authority. As can be seen in Figure 2, the coverage of the data is focused on the SNS where most of the gas reserves are found and sourced from the underlying Carboniferous.

The quantity and quality of the seismic data have permitted the detailed time and depth mapping of the major stratigraphic boundaries down to the base Zechstein. Deeper Carboniferous and Devonian structures are however more difficult to seismically image due to the presence of both the overlying stratigraphic layers, in particular the Zechstein evaporite layers and associated structures as well as legacy processing designed to only image down to the base Zechstein (top of the basal Permian sandstones). Since many of the gas reserves found in the SNS are sourced from the Carboniferous, the major aim of this study is to improve our understanding of the regional structure and tectonics of the Carboniferous basin by applying the 'gravity layer stripping method'. This may help to identify, as yet, undiscovered, commercial gas reserves.

The 'gravity layer stripping method' uses a ~5 km minimum (half wavelength) resolution satellite derived, sea-level, free air anomaly (FAA) gravity dataset (Green *et al.* 2019) for the UK sector of the North Sea (data available from the North Sea Transition Authority). From this sea-level FAA gravity field, the summed gravity response of the sea water layer plus each of the identified four stratigraphic layers (Fig. 3) down to the base Zechstein have

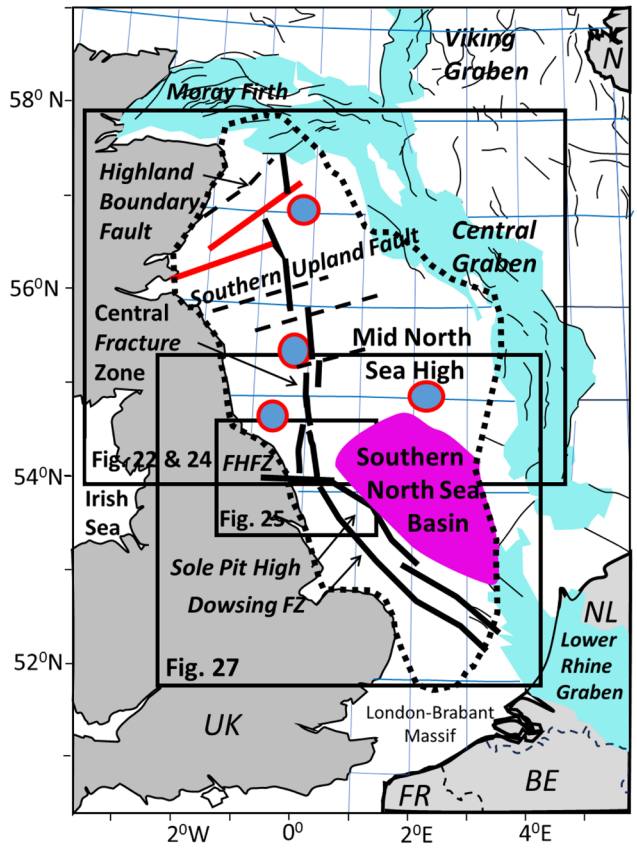

Fig. 1. Summary geology map of the UK sector of the North Sea showing and naming the main structures identified by the BGS and this study (Figs 22, 24c, respectively). These structural elements have been superimposed on Tertiary related maps of Figures 6, 7 and 17. The outline locations of Figures 22, 24, 25 and 27 are shown. Red lineaments probably magmatic in origin, red outlined blue dots are granites and FHFZ is Flamborough Head Fault Zone.

been removed to generate the residual gravity field response, at the sea surface, of the largely Carboniferous and deeper crustal density structures down to the Moho. The spatial variation in the gravity response of the Moho density discontinuity was also removed from the residual gravity field.

Figure 3 shows the sea water layer and the 4-stratigraphic layers which have been stripped from the FAA to generate the 'sub-Zechstein residual crustal gravity field' (the Moho discontinuity is not shown). This aims to image all lateral and depth variations of density below the base Zechstein surface and includes density variations within the Carboniferous (rocks with higher or lower density than the assumed average Carboniferous density of 2.6 g cm^{-3}) as well as the structure of the base Carboniferous and sub-Carboniferous structures down to the Moho.

To generate an accurate 'sub-Zechstein residual crustal gravity field' response, the following 'gravity layer stripping method' workflow (Fig. 4) has been used. Each workflow section forms a separate text section.

If the gravity response of the Moho density discontinuity is not removed from the sub-Zechstein residual crustal gravity field, it will be strongly affected by the eastward thinning of the crust due to the shallowing of the Moho density boundary towards the centre of the North Sea basin. To minimize this regional gravity effect, an Isostatic correction was applied based on an existing model of Moho depth.

The Gravity, depth and average-interval-velocity grids section describes the construction of the seismically derived depth and two-way-time (TWT) grids for each of the stratigraphic layer interfaces and their merging to generate the average-interval-velocity (AIV) grids for each layer. Except for the construction of these depth and TWT grids, undertaken by one of the authors (DM), the work presented here is the result of MSc summer project studies carried out by Azli (2018), Özsöz (2019), Maxwell (2020), Zhang (2020) and Rose (2022) supervised by the other co-authors.

Since the majority of wells have been logged in ft and ft/sec since 1964 these units have been retained and clearly identified in map images and figures. The conversion factor to metres is 1 ft = 0.3048 m. Grid images used in this paper are 100% colour equalized with shaded relief illuminated from the NE.

Gravity, depth and average-interval-velocity grids

Free air anomaly gravity grid

The free air anomaly (FAA) gravity grid, used in this study, is the Multi-Sat 2016 solution (Green *et al.* 2019). It is constructed from radar altimeter data from 5 geodetic satellite missions (with Cyrosat-2 having multiple operational modes), all orbiting the Earth at

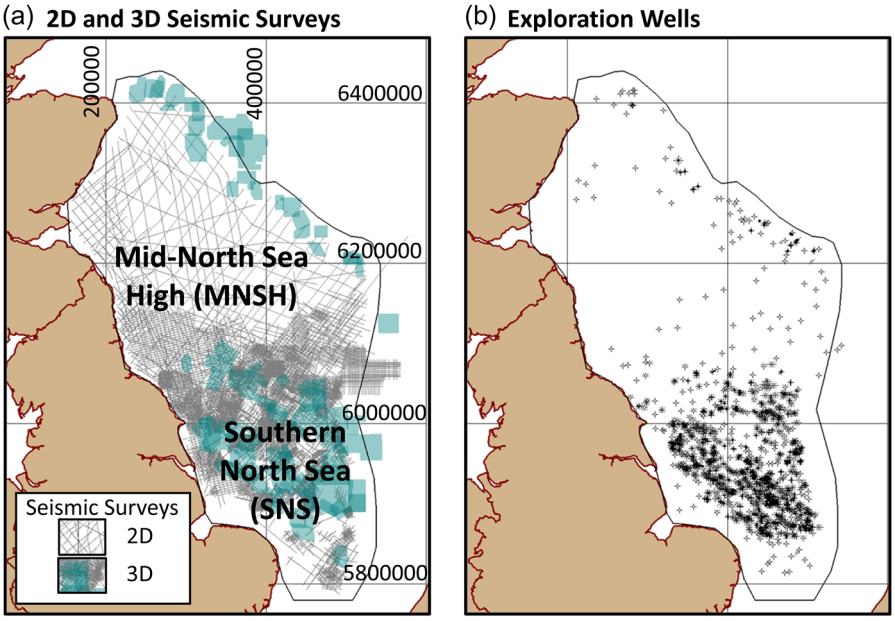

Fig. 2. (**a**) 2D and 3D seismic survey coverage of the UK sector of the North Sea and (**b**) coverage of 785 available wells. Coordinate system used is UTM31 (ED50) with grid origin of −60 000, 5 004 000 m.

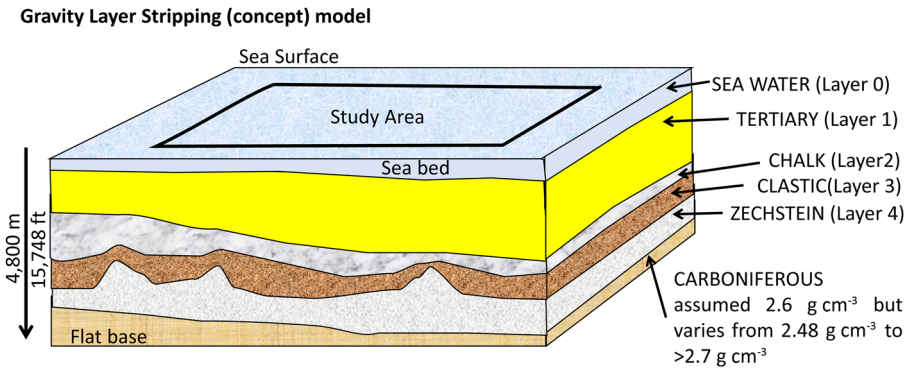

Fig. 3. Schematic layer-cake model used in the 'gravity layer stripping method' which for this study involves a sea water layer and 4 density layers (excluding Carboniferous). The gravity response for each layer and the Moho discontinuity were calculated, summed and removed from the Free air gravity to generate the 'sub-Zechstein residual crustal gravity field'.

heights 720–1330 km (Fig. 5). These satellites have a range of orbital inclinations, so by combining the along track data the effective ground track spacing has progressively decreased (i.e. spatial resolution increased) with time as data from new satellites has become available. The Multi-Sat 2016 solution has an average track spacing of less than 2 km at the Equator, whilst farther north and south from the Equator the track spacing decreases to ~1 km for the North Sea.

Figure 5a shows the individual coverage of the 5 satellites for a small section of the SNS, as of 2016, as well as their combined coverage. The resulting FAA gravity solution (Fig. 5b) is thus based on an average track spacing of about 1 km and has a resolution down to ~5 km half wavelength (Green *et al.* 2019). The spatial resolution of the Multi-Sat 2016 data has been tested over the MNSH (Fig. 1) against the EDCON-PRJ (2015) and the legacy (1968–90) British Geological Survey (BGS) marine gravity surveys (Kimbell and Williamson 2015). These marine surveys had orthogonal NE–SW & NW–SE ship tracks with line spacings of ~15 km and north–south & west–east ship tracks with line spacings of ~10 km, respectively. The grid based spatial resolution of the satellite derived solution was found to be at least equivalent if not superior to the wide line spacing of these marine surveys (Azli 2018), although the shipborne data have higher resolution along line.

Layer depth and TWT grids

The depth to the layer interfaces requires both the TWT and AIV grids for each layer to be determined. However, for the sea water layer, the seabed interface is often not imaged, or very poorly imaged by seismic data acquired for hydrocarbon exploration throughout the area. Thus, the bathymetry grid used was the 2016 version of the EMODnet DTM which has a grid spacing of 1/8 × 1/8 arc minutes, (or ~200 m × 200 m) (https://emodnet.ec.europa.eu). This depth grid was gridded to a 100 m × 100 m cell size, and used in this study. Since the grid was not tied to any fixed bathymetry data points, it was flexed to tie with the bathymetry values at the wells. For depth conversion, the bathymetry grid is required to be in the form of seismic TWT. This was done using an average seawater velocity of 4850 ft/sec within the study area containing the MNSH and SNS areas (Fig. 2a).

Throughout the UK sector of the North Sea there are four regional sub-seabed boundaries that can be mapped on seismic data for all vintages since the early 1980s. These are:

base of the Tertiary clastic sequence/top Cretaceous Chalk,
base Cretaceous Chalk,
base Clastic or top Permian Zechstein and
base Permian Zechstein.

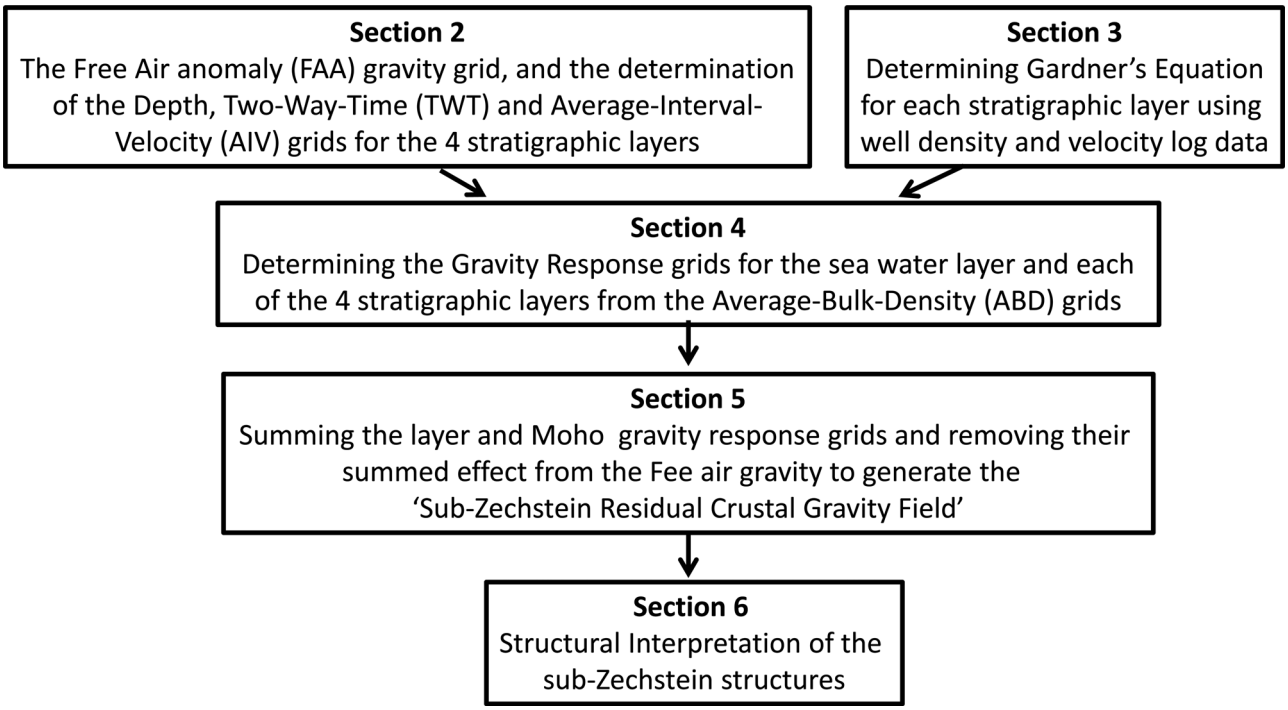

Fig. 4. Workflow used in the 'gravity layer stripping method' to investigate the Carboniferous geology and structure in the UK sector of the Mid North Sea High (MNSH) and the Southern North Sea (SNS).

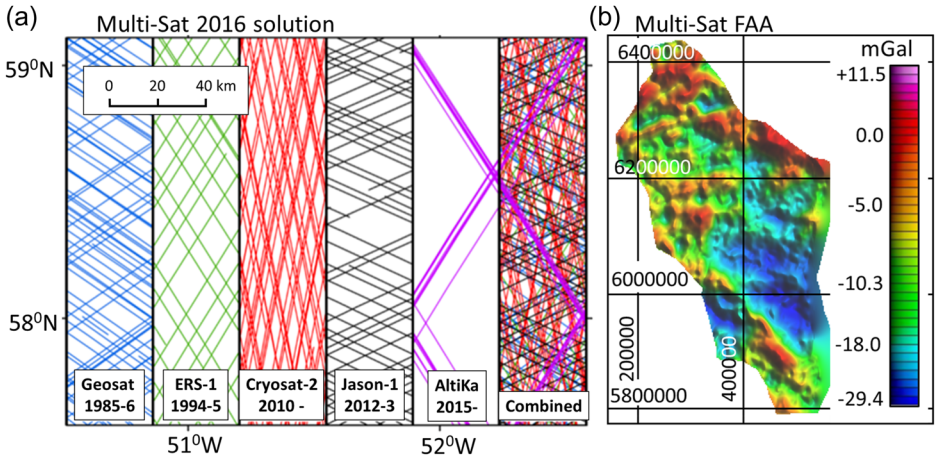

Fig. 5. (**a**) Track spacings of 5 geodetic radar altimeter satellites since 1985 and the combined coverage that gives a ~1 km spacing for the SNS, (**b**) the free air gravity anomaly (FAA) for the UK sector of the North Sea.

The seismic TWTs to these boundaries were picked to tie with the well velocity survey times from 785 wells. The time grids for each of the four boundaries had cell sizes of 100 m × 100 m to match the bathymetry grid. From these time grids (not shown), isochron grids were generated for the Tertiary clastic sequence, the Cretaceous Chalk interval, the interval from the base of the Chalk formation to the top of the Permian Zechstein formation and for the Permian Zechstein interval. The interval between base Cretaceous Chalk and top Permian Zechstein comprises Lower Cretaceous shale, Jurassic which is largely Lias and middle Triassic with halite layers and Lower Triassic Bunter sandstone. With very few exceptions, the Halite is not caught up in any Zechstein salt intrusions.

The well velocity survey data were then used to derive seismic travel time–well depth functions to predict the isopachs from the isochrons for each of the 4-layer intervals. The functions and their parameters were selected so they minimized the RMS depth conversion errors. It should be noted that well data values are not a perfect fit to any derived function, such that the resulting depth grids, obtained by summing the isopach grids, will not tie to the well depth precisely. To minimize depth errors, for each layer in turn, the depth grid for the base of the layer is flexed to tie with the well depths. The resulting depth and thickness grids are shown in Figures 6 and 7, respectively.

In the SNS area, there are many wells and widespread 3D seismic coverage (Fig. 2), most of the depth conversions are accurate to better than 100 m so that the degree of grid flexing is relatively small. The depth and TWT grids were then used to determine the average-interval-velocity (AIV) at each grid node for each of the 4 stratigraphic layers where:

$$\mathrm{AIV} = \frac{2(X_2 - X_1)}{T_2 - T_1} \quad (1)$$

where X_1 = depth to top of layer, X_2 = depth to bottom of layer, T_1 = TWT to top of layer and T_2 = TWT to bottom of layer.

To convert the laterally varying AIV grids (Fig. 8) to average-bulk-density (ABD) grids, the density–interval velocity function used the Gardner's function (equation 2, Gardner *et al.* 1974) with a (Gardner's coefficient) and m (Gardner's power) determined for each layer using well density and velocity data (see the Determining Gardner's equation for each stratigraphic layer section). For each layer, ABD values can then be derived at each grid node from Gardner's function using the AIV grid. Since the 100 m × 100 m average density grids are considerably finer than the spatial resolution of the satellite gravity data (see the Free air anomaly gravity grid section) the gravity response was derived on a 4 km cell size grid.

Determining Gardner's equation for each stratigraphic layer

Density well log processing

The distribution of the density well log datasets for the UK sector for the North Sea is far from uniform (Fig. 2a), particularly over the MNSH, so extrapolation/interpolation of the well density results generates unacceptable grid solutions (Kimbell and Williamson 2015; Azli 2018). In Kimbell and Williamson (2015) study of the MNSH, they used a predictive approach to determine the density after Japsen (1998, 1999, 2000) based on an understanding of compaction trends and the relationship between thickness and average density in the evaporitic Zechstein sequence. The method used here, was to convert the average-interval-velocity (AIV) values at each grid node for each layer to average-bulk-density (ABD) values (equation 1 and Fig. 8) using the derived Gardner's equations (Maxwell 2020; Rose 2022). By using the AIV grid approach, interpolation between widely spaced well depth and velocity values is more accurate, provides good estimates of the ABD at grid nodes for a layer and removes the need to consider poorly known spatially varying density–depth gradients for individual layers.

To achieve this, well density logs need to be processed in two stages after removal of anomalous and spurious density values. The sampling problem is clearly demonstrated for well logs shown in Figures 9, 10. In Figure 9, the density–depth plot for well 49/14a-2 samples the Tertiary and Cretaceous Chalk layers and is shown before and after the application of stage 1 filter which removes all density values exceeding ±0.1 g cm^{-3} about the average. This stage 1 smoothing used a convolution filter to determine the average.

In addition to the two stages of filtering, initial processing of the well log data also involved the removal of a few extreme density (and velocity) values. Low density values could be due to borehole caving/cavities and high densities due to localized thin formations such as siderite.

By trial and error, the best results for stage 1 filtering were obtained using a window containing 200 density values and only retaining density values within ±0.1 g cm^{-3} limits of the average. This stage 1 filtering basically cleans up the data without removing stratigraphic layers that are present. To reduce the quantity of data per well further, a stage 2 filter was applied to only recover average sample values every ~100 m down the log. This process is considered to reduce the effect of data clustering and biasing due to increased sampling at certain depths. The filtering thus helps to produce a function that helps to represent the layer.

The Zechstein density logs reveal a broad range of densities due to the presence of low density (~2.1 g cm^{-3}) halite and high density (~2.9 g cm^{-3}) anhydrite as well as limestones and dolomites with

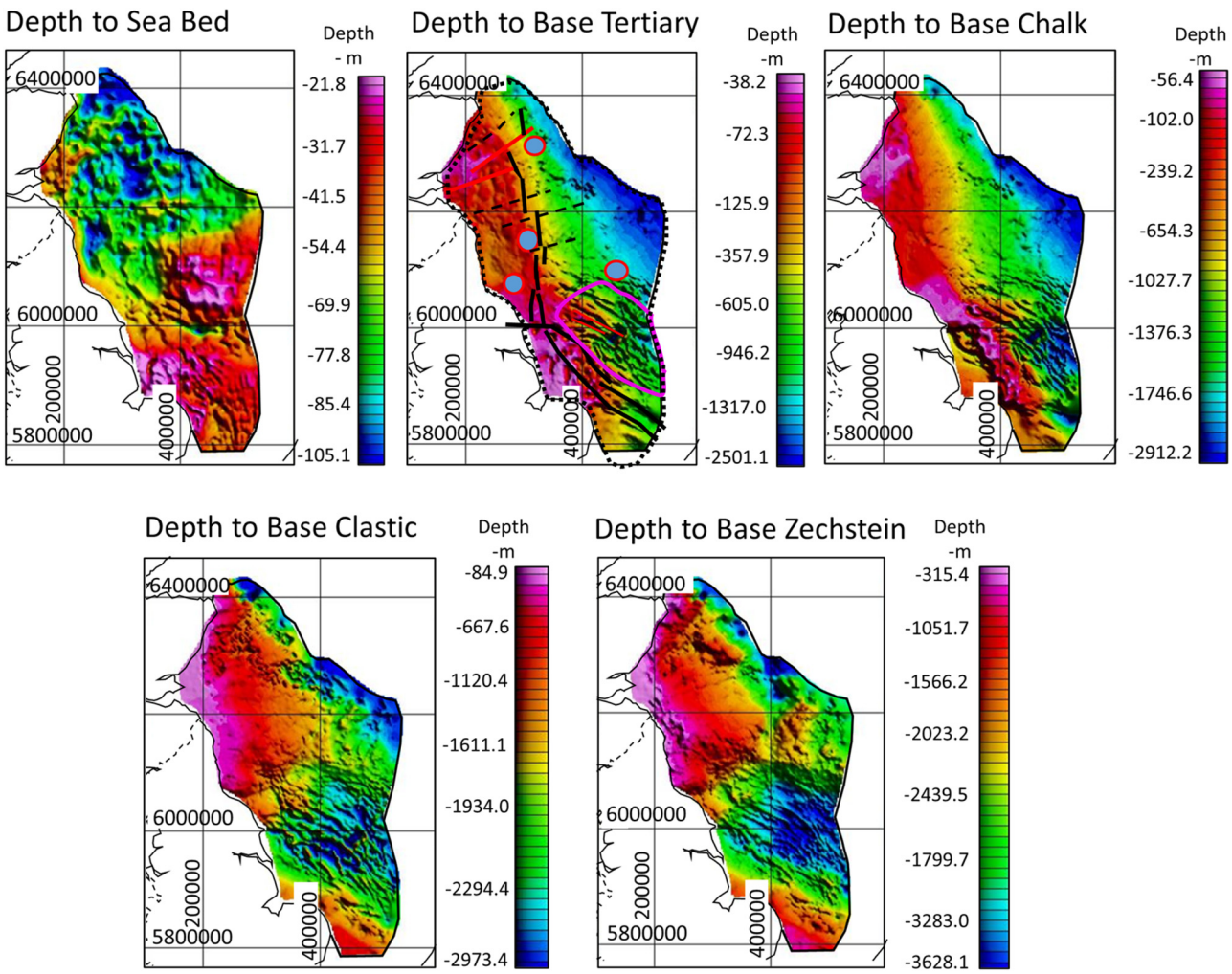

Fig. 6. Depth maps of the sea bed and the 4 stratigraphic layers in metres used in the 'gravity layer stripping method'. The interpretation structures (shown in Fig. 1) have been superimposed onto the depth of base Tertiary map.

densities of around 2.7 g cm^{-3}. To determine the average density Kimbell and Williamson (2015) in their study used a well log cross-plot of average density against thickness which showed an inverse relationship, with the average density increasing as thickness decreases, reflecting the greater proportion of halite in the thick evaporitic sequences. In this study the AIV at each grid node was used to determine the ABD value.

For the pre-Zechstein (Carboniferous and Devonian), Kimbell and Williamson (2015) show that the overall average density of the pre-Zechstein rocks in sampled sections is 2.557 g cm^{-3}, and the average densities within individual wells range from 2.29 to 2.71 g cm^{-3}. So, the assumed background density used in this study for the Carboniferous of 2.6 g cm^{-3} is reasonable (Fig. 11). Since the late Carboniferous rocks contained in the SNS are made up of substantial thicknesses of Westphalian strata deposited between 315 and 296 Ma (Westphalian rocks previously collectively referred to as Coal Measures) have densities less than 2.6 g cm^{-3}, they will appear as areas of negative anomaly in the Carboniferous Isostatic anomaly.

According to BGS studies, the basement beneath the MNSH region comprises metamorphosed Lower Paleozoic rocks and crystalline basement intruded by Devonian granites. Based on onshore equivalents, the average basement density for the Southern Uplands is about 2.72 g cm^{-3} but ranges from around 2.70 g cm^{-3} for the quartz-rich units to 2.75 g cm^{-3} for denser lithologies. In northern England, the average basement densities range from about 2.72 g cm^{-3} for Silurian rocks to 2.78 g cm^{-3} for Ordovician rocks (Kimbell *et al.* 2006 and references therein).

Velocity well log data

The density spikes seen in Figures 9 and 10, are associated with lithology variations and changes in sonic velocities. An example is shown in Figure 12 for the velocity log from 10 000 to 10 500 ft *(3048 to 3200 m)* of well 44/28-4 for a high velocity spike seen in the mid Zechstein layer in Figure 10. The two logs on the left of Figure 12 are the gamma ray log which is used to correlate between well logs and the sonic log. The two curves on the right are the velocity logs before and after calibration, with the dashed line showing where the calibration had been adjusted to the integrated sonic values. The two sets of tick marks are the integrated times. The ones to the right are the one-way times before the adjustments and the more closely spaced tick marks are the two-way seismic times after calibration. The time difference between two tick marks is 1 ms transit time for the seismic energy. The log is derived from the sonic log which has a 6-inch *(0.15 m)* sample interval and the seismic VSP survey with a sampling interval of 300 ft *(91 m)*. Processing of these data first removes both positive and negative noise spikes from the sonic log and the raw VSP time values are corrected for source and receiver depths at the sea surface plus a correction for bending of ray paths as they pass through the acoustic impedance boundaries in the subsurface. The integrated sonic log travel times are then adjusted to match the corrected VSP times. The resulting velocity log is considered to be 'noise' free. All variations on the log are geological, lithology variations. As shown in Figure 12, the high velocity between 10 120 and 10 220 ft (*3085*

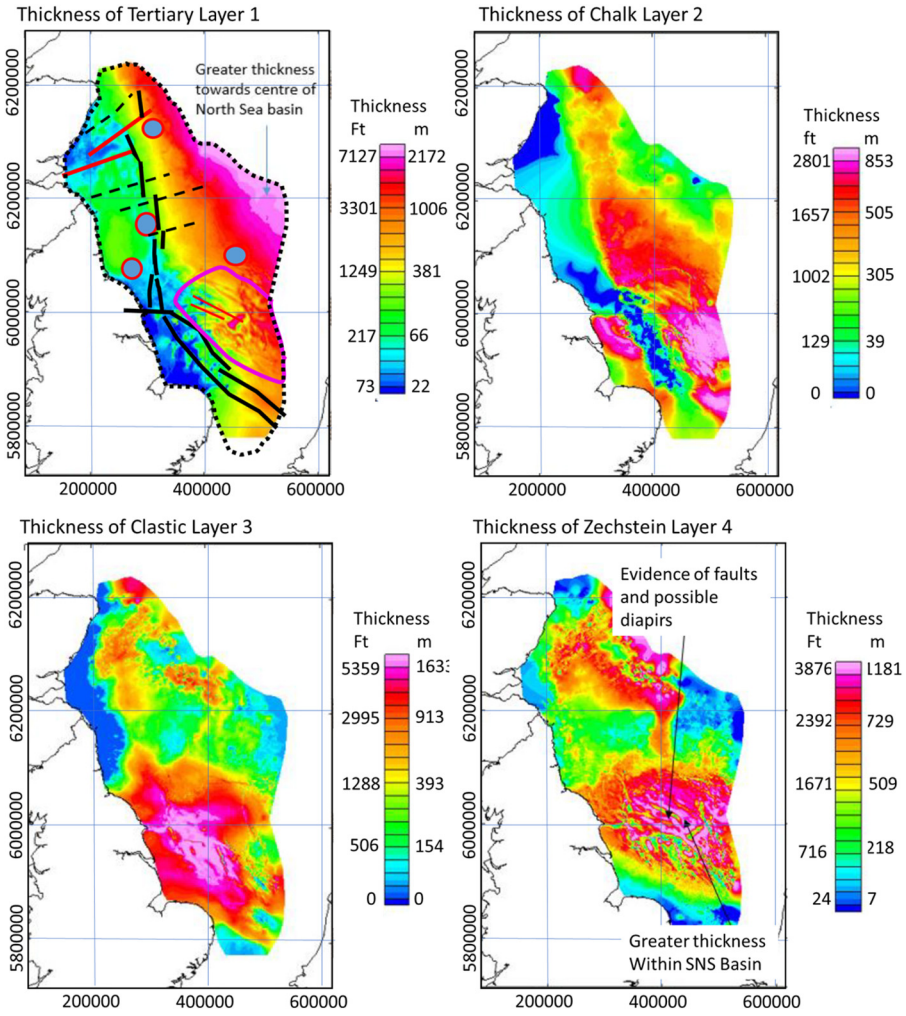

Fig. 7. Layer thickness maps for the UK sector of the North Sea based on layer depth maps shown in Figure 6. To relate the interpretation structures (shown in Fig. 1) to the layer thickness maps, they have been superimposed onto the Thickness of the Tertiary Layer 1 map.

and 3115 m) is a layer of anhydrite; the next 20 ft (*6 m*) is dolomites and below that 60 ft (*18 m*) of marly Stassfurt halite.

Gardner's equation & density–velocity plots

To convert an AIV grid into an ABD grid, described in the layer depth and TWT grids section, the empirical derived Gardner's equation (Gardner *et al.* 1974) has been used which determines the relationship between density and velocity for each lithologic layer down to the base (Permian) Zechstein strata. The Gardner's equation is defined as

$$\rho = aV^m \tag{2}$$

where ρ = bulk density, a = Gardner's coefficient, V = seismic P-wave velocity, m = Gardner's power. Gardner *et al.* (1974) proposed that one could obtain a good fit by applying this equation to sedimentary rocks using the default values of

$a = 0.23$ and $m = 0.25$ where V is in ft s^{-1} (used in this study) or
$a = 0.31$ and $m = 0.25$ where V is in m s^{-1}

Since the physical properties of the geology within a sedimentary layer can vary both laterally and vertically, as clearly seen for the North Sea logs (Figs 9, 10), the values of a and m can also vary, thus they have been calibrated in this study from the available sonic and density well log information for each of the 4 layers.

Other functions have been proposed by Brocher (2005), Christensen and Mooney (1995) and Sobolev and Babeyko (1994) but Gardner's equation is preferred for sedimentary basin studies. The default values of Gardner's equation are found to be a reasonable approximation for sand–shale lithologies but do vary with lithology as shown by Nwozor *et al.* (2017) for the Niger Delta, Quijada and Stewart (2007), for Manitou Lake, Saskatchewan and by Filina *et al.* (2014) for the Gulf of Mexico. It should be noted that despite Gardner's equation and its default values being good approximations for sedimentary basins containing sandstones and carbonates, the coals and evaporites, present in the North Sea basin, display different velocity–density relationships (Quijada and Stewart 2007).

In this study, the values of a and m in equation (2) were determined from density–velocity plots for each layer (Figs 13–16) by determining the best fit Gardner's equation to these datasets. This was done by minimizing the sum of the residual error squared (sum Chi squared).

To obtain the best fit, the effects of data bias and clustering have to be minimized. This was done using the two-stage filtering process described in the Density well log processing section.

Gardner's function for the Tertiary (Cenozoic) Layer 1: Figure 13a shows all the density and velocity data from 25 well logs for the Tertiary (Cenozoic) Layer 1, after removal of extreme density and velocity values. Figure 13b shows the data plot after the two-stage filtering. As one can see there is a dramatic 75% reduction of data points allowing a clearer trend to be identified. The Gardner's function is shown in each image and tabulated in Table 1.

On closer inspection of Figure 13, some clusters of data points appear to show their own Gardner's trends. This suggests that a more effective way to process the data would be to design a Gardner's function for each area of the layer with its own unique relationship. This is beyond the scope of the study and also requires a good uniform coverage of well logs that does not exist. The majority of the data conform to sandstone with the lesser trend

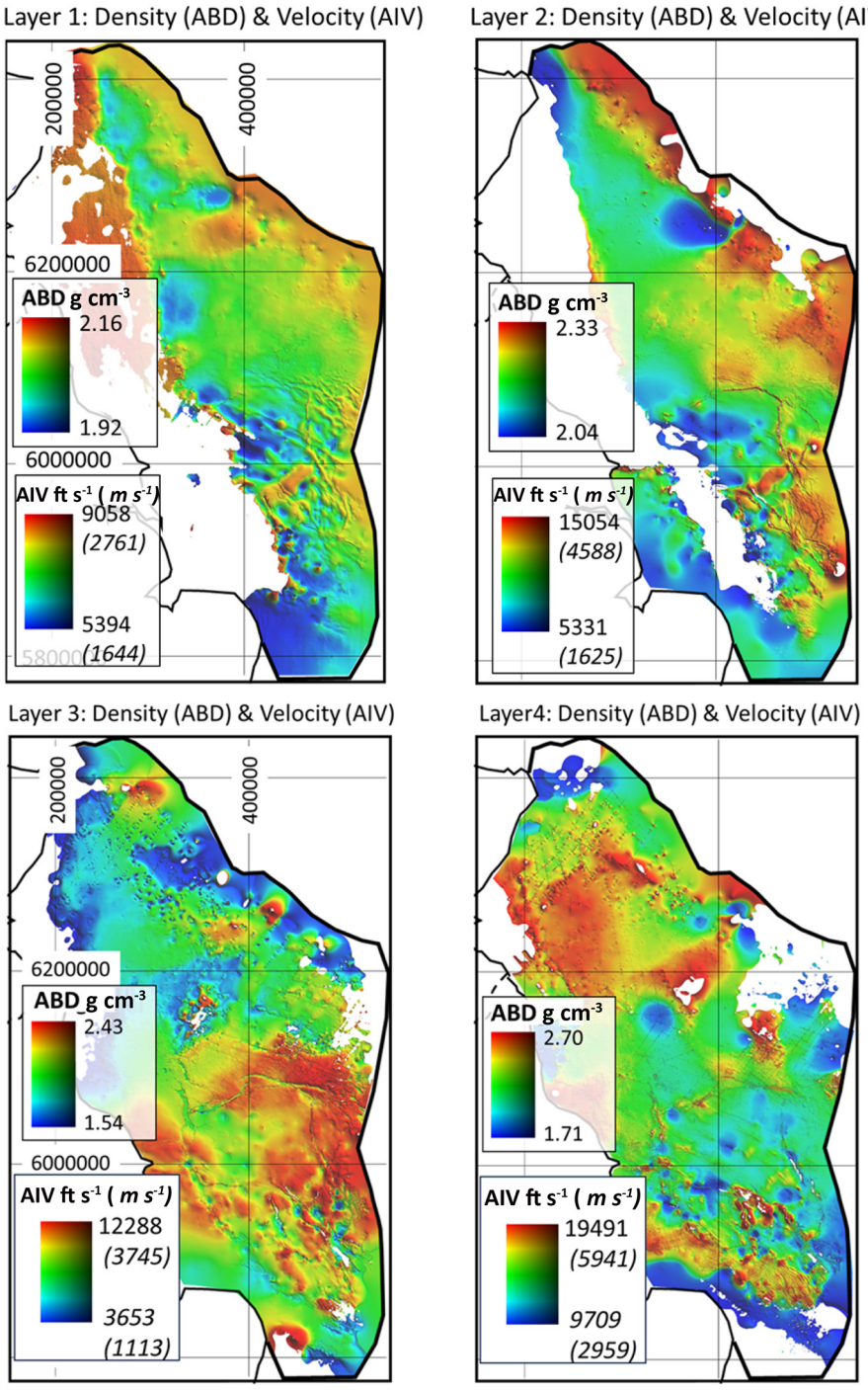

Fig. 8. The average-interval-velocity (AIV) and average-bulk-density (ABD) maps of the 4 layers. Since these two sets of maps are linked by Gardner's function (different for each layer) only the colour legends are different. White areas represent areas lacking sediments due to erosion or non-deposition.

possibly being due to wet sand. These rock types are to be expected of the Tertiary (Cenozoic) due to them being a young formation resulting in a lack of compaction and therefore wet sand.

The above features, seen in Figure 13, are borne out by the geology. In the northeastern part of the SNS in the UK sector there is a Pliocene deltaic formation prograding from the east overlying a mid-Miocene unconformity which has eroded out lower Miocene and most of the Oligocene section leaving low velocity relatively unconsolidated sandy section overlying consolidated shales of Eocene age. This sharp velocity hiatus within the Tertiary makes application of Gardners' equation to the whole Tertiary interval problematic. In Figure 10 the low-density layer near the surface is the result of Pliocene on Eocene section. The problem is exacerbated since going westward out of the basin, sees older and older Tertiary section sub cropping the seabed. The current model for the Tertiary layer is not ideal since the study lacks a regional structure map for the mid-Miocene unconformity. Given the sparse logging of the shallow near-surface Tertiary section these variations within the Tertiary sequence help to explain the observed clusters of Tertiary data in Figure 13b.

Gardner's function for the Cretaceous Chalk Layer 2: Layer 2 is similar to layer 1 with a clear trend of increasing density with velocity (Fig. 14). Filtering helps to define the trend (Fig. 14b). Two data clusters are prominent centred approximately on 2.0 g cm^{-3}, 7000 ft s^{-1} (*2134 m* s^{-1}) and 2.4 g cm^{-3}, 14 000 ft s^{-1} (*4267 m* s^{-1}). Some of the data points appear unreasonable but over compaction has been cited as a source of higher velocities in the south (the Netherlands area of the North Sea), with velocities up to 18 000 ft s^{-1} (*5486 m* s^{-1}), due to uplift (Van Der Molen 2004). This is the case with the southern part of the study area. Van der Molen (2004) also found that burial depth was the primary control on the level of compaction.

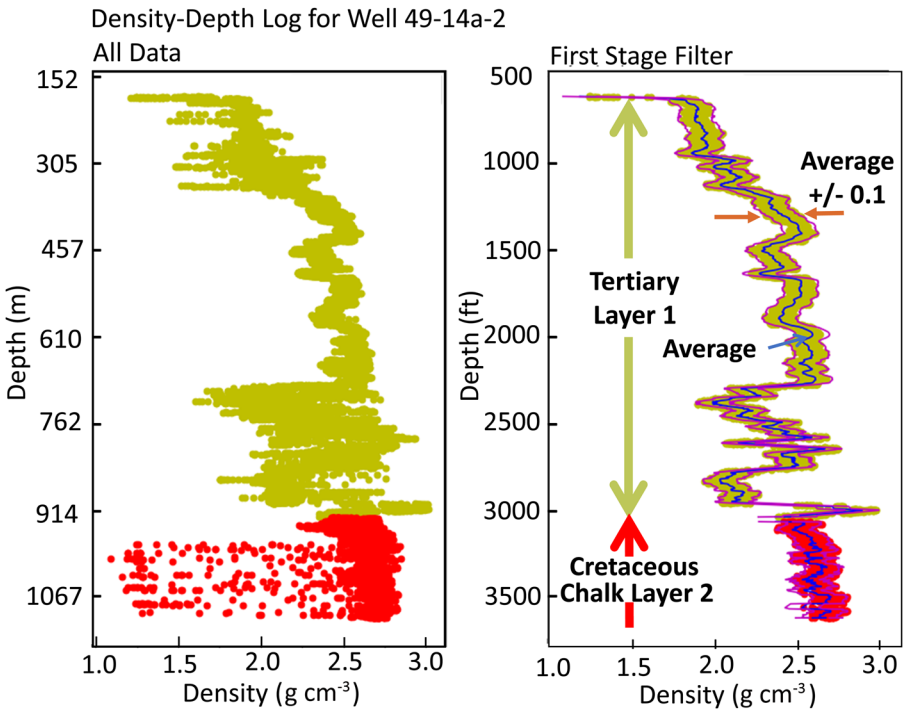

Fig. 9. Density–depth plot for well 49/14a-2 (53.51096 (latitude) 2.69875 (longitude)) for the upper two layers, Tertiary and Cretaceous Chalk. (**a**) 'All Data' plot shows a large number of lower density values in the Cretaceous Chalk layer 2, (**b**) first stage filtered data showing point values within the ±0.1 g cm^{-3} limits of the rolling average.

Gardner's function for the Clastic Layer 3: The clastic layer comprises the lower Cretaceous, when present, the Jurassic, largely Lias shales when present, Upper and Middle Triassic section which is a mixed lithology of sands, shales and halites, and lower Bacton Bunter sandstone. The clastic layer is texturally and lithologically similar to layer 1 (sandstones), but having, on average, greater velocities, and densities due to their greater depth causing compaction (Fig. 15). The average density of all data is 2.37 g cm^{-3} compared with 2.13 g cm^{-3} for layer 1 (Table 1). On filtering the data points (Fig. 15b), the average densities change to 2.41 g cm^{-3} and 2.07 g cm^{-3}, respectively.

Gardner's function for the Permian Zechstein Layer 4: The Zechstein layer is perhaps the least well modelled layer using the Gardner's equation. This is because the anhydrite at the top of the layer and the halite at the bottom are not well modelled by Gardner's function. This is reflected in the density–velocity plot of Figure 16b, where the carbonate between 1.7–2.6 g cm^{-3} and 13 000–18 000 ft s^{-1} (*3962–5486 m s^{-1}*) shows a clear increase in density with velocity, but the halite 2.1 g cm^{-3} and anhydrite 2.9 g cm^{-3} show no increase in density with velocity.

Gardner's equation uncertainties

The uncertainties in the *a* and *m* values within the Gardner's function (equation 2) can be determined by manual adjustment of values for visual best fitting curves, or (ii) adjusting the values to minimize the errors by comparing the density data to density estimates obtained from sonic velocities (Nwozor *et al.* 2017).

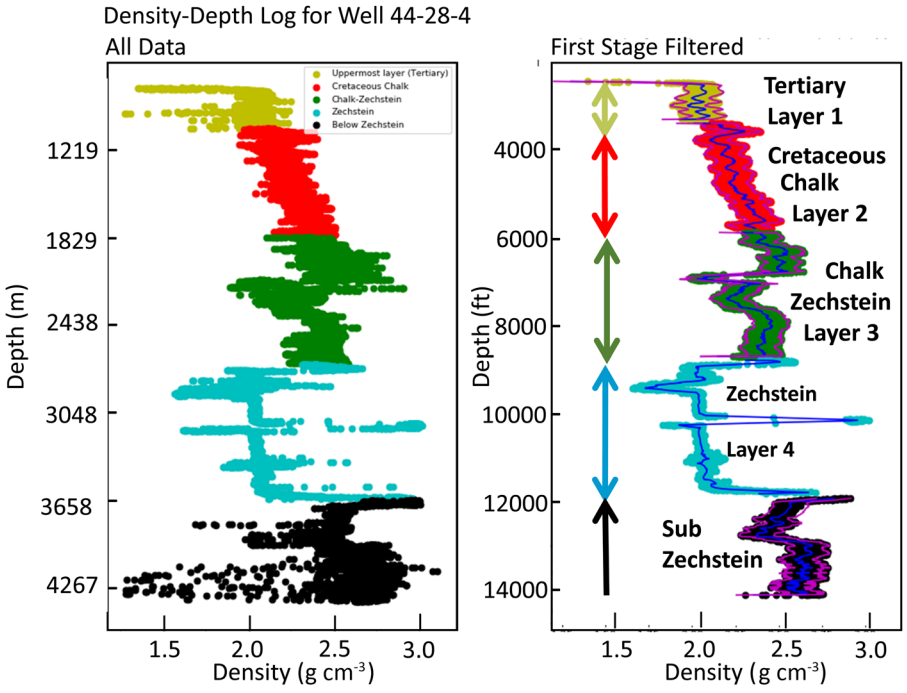

Fig. 10. Density–depth plot for well 44/28-4 (54.12094 (latitude) 2.40600 (longitude)) for all 4 layers and sub-Zechstein. (**a**) 'All Data' show a large number of high-density values in the Zechstein layer and low-density values in the Tertiary and sub-Zechstein /Carboniferous, (**b**) first stage filtered data showing all data points within ±0.1 g cm^{-3} limits together with the rolling average line.

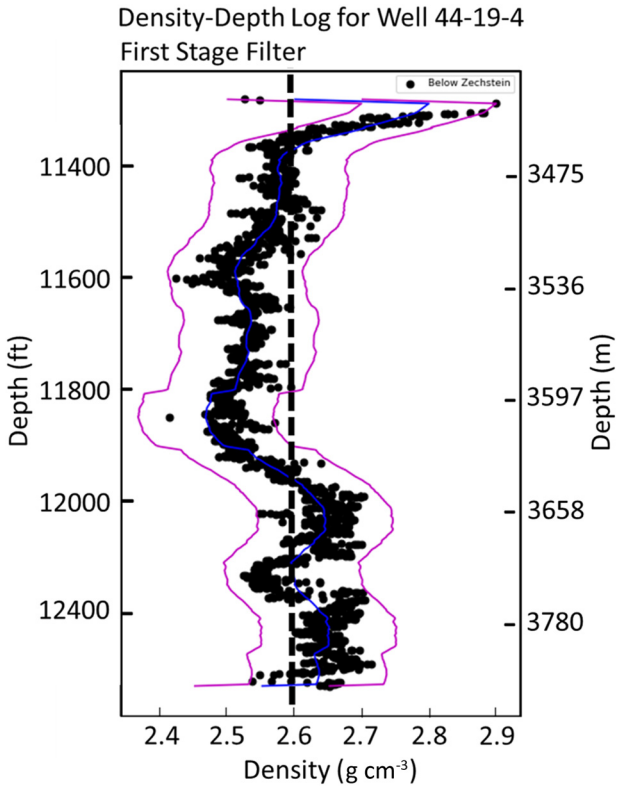

Fig. 11. Density–depth plot after stage 1 filtering for well 44/19-4 (54.44651 (latitude) 2.77599 (longitude)) showing the density variation within the Carboniferous. For completeness, the rolling average and the ±0.1 g cm^{-3} limits are shown.

Two methods are used here to measure the uncertainty. The first method is Summing the Square Residuals (*SSR*) which defines how close the Gardner's function matches the data. If the *SSR* value is small, it means that the function matches the data well.

$$SSR = \sum (\text{measured densities} - \text{predicted densities})^2 \quad (3)$$

The second method is to measure the uncertainty using linear regression, and determining the R^2 value, which is the square of the correlation coefficient. If this value is found to be high (closer to 1), in contrast to the *SSR*, it suggests the data is well correlated with the function.

$$R^2 = 1 - \frac{SSR}{SST} = 1 - \frac{\sum (y_i - y_p)^2}{\sum (y_i - y_m)^2} \quad (4)$$

where *SSR* = sum of squared regression, *SST* = sum of squares total, y_p = predicted value, y_m = mean of all values and y_i = measured value.

Table 1 gives the derived values of Gardner's coefficients, *a*, and power, *m*, for each layer as well as their *SSR* and R^2 values.

Some interesting inferences can be made from the analysis of Table 1. The coefficient and power for layers 1 and 2 appear to change very little after application of the first stage smoothing but the subsequent depth averaging caused larger changes. By contrast the processing steps only made small changes to the function for layer 4. The final values of Gardner's functions determined appear reasonable and what could be expected of a sedimentary basin. The *SSR* values decrease as expected after each step of the processing as the spurious data points are removed. The one exception to this trend was the application of depth averaging to layer 4 data, where there was a small increase in the *SSR*.

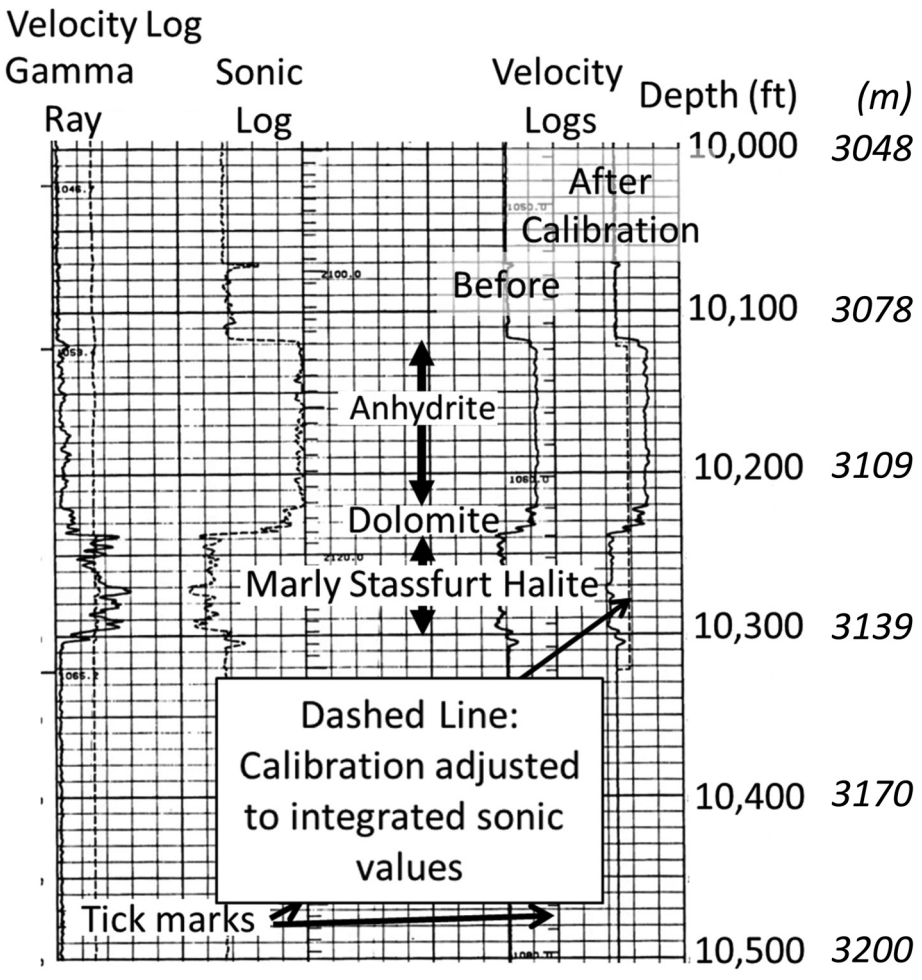

Fig. 12. Velocity log for the section between 10 000 and 10 500 ft *(3048–3200 m)* for well 44/28-4, illustrating the high velocity spike seen in the mid Zechstein in Figure 10.

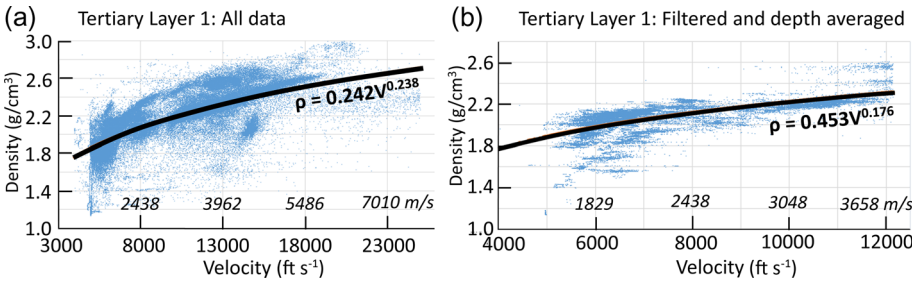

Fig. 13. Gardner's relation between density and velocity data for the Tertiary (Cenozoic) Layer 1. (**a**) Plot of all data for 25 well log density and velocity data (144 737 data points), (**b**) plot of same data after filtering and depth averaging (36 679 data points, a reduction of 75%). See Table 1 for full statistics.

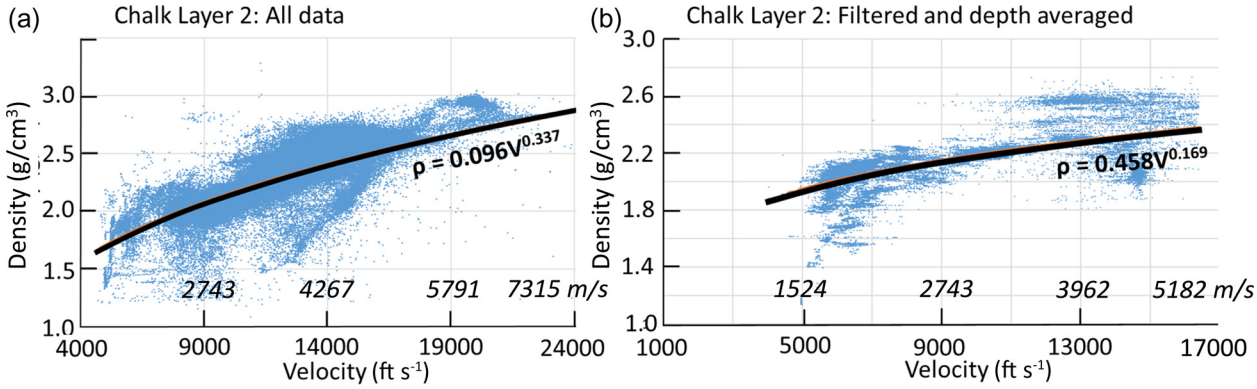

Fig. 14. Gardner's relation between density and velocity data for the Cretaceous Chalk Layer 2. (**a**) Plot of all data for 29 well log density and velocity data, (**b**) plot of same data after filtering and depth averaging. See Table 1 for full statistics.

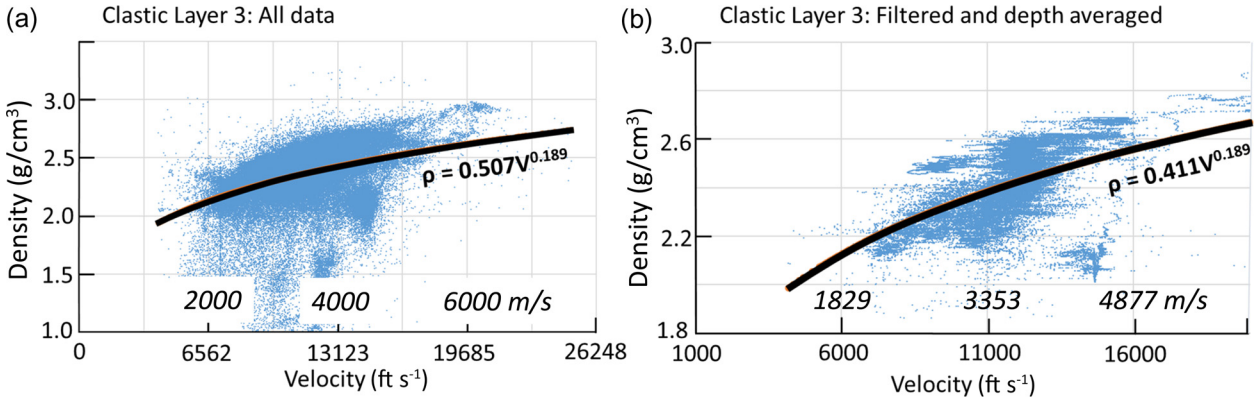

Fig. 15. Gardner's relation between density and velocity data for the clastic Layer 3. (**a**) Plot of all data for 42 well log density and velocity data, (**b**) plot of same data after filtering and depth averaging. See Table 1 for full statistics.

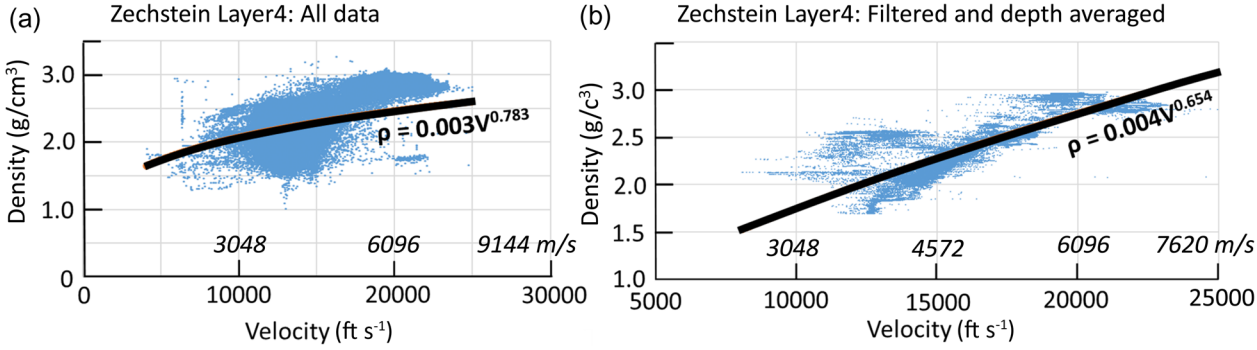

Fig. 16. Gardner's relation between density and velocity data for the Zechstein Layer 4. (**a**) Plot of all data for 53 well log density and velocity data, (**b**) plot of same data after filtering and depth averaging. See Table 1 for full statistics.

Table 1. Gardner's function values and uncertainties for each of the 4 layers in the UK sector of the North Sea

DATA	Gardner's equation				Number of wells	Number of data points	% Reduction data points	Average density g cm^{-3}
	a (ft s^{-1})	Power	*SSR*	R squared				
Layer 1 Tertiary					25			
All data	0.242	0.238	0.209	0.4991		144 737		2.13
Stage 1 filter smoothing	0.25	0.235	0.193	0.5264		122 755	15	2.13
Stage 2 filter data averaging	0.453	0.176	0.121	0.4133		36 679	75	2.07
Layer 2 Cretaceous Chalk					29			
All data	0.096	0.337	0.179	0.5245		170 103		2.27
Stage 1 filter smoothing	0.117	0.316	0.158	0.5337		146 195	14	2.27
Stage 2 filter data averaging	0.458	0.169	0.151	0.4018		47 979	72	2.12
Layer 3 Clastics					42			
All data	0.507	0.189	0.225	0.113		202 488		2.37
Stage 1 filter smoothing	0.585	0.151	0.182	0.1002		154 735	24	2.4
Stage 2 filter data averaging	0.411	0.189	0.131	0.2377		56 187	72	2.41
Layer 4 Permian Zechstein					53			
All data	0.003	0.783	0.218	0.6553		229 897		2.29
Stage 1 filter smoothing	0.003	0.794	0.198	0.6984		181 989	21	2.28
Stage 2 filter data averaging	0.004	0.654	0.209	0.5735		66 288	71	2.35

The variation in the R^2 values, in Table 1, were more unexpected. The values are not large but do increase following the stage 1 smoothing. This was expected since more extreme values are removed in the stage 1 filtering. However, the values decrease following the stage 2 depth averaging. This is likely because stage 2 depth averaging removed values that were already close to the function.

In summary, this analysis does show that Gardner's functions represent the data more closely following each processing step.

Determining the bulk density and gravity response grids for each layer

As previously described, the ABD grids for each layer were determined from the AIV grids using Gardner's equation *a* and *m* values (Table 1). That is, for a given layer, each grid node of the AIV grid (Fig. 8), is used to derive an ABD value (Fig. 8). Since the two grids are linked by a Gardner's equation, the ABD and AIV colour grids are identical but vary in their colour bar values.

Figure 17 shows grid images of the gravity response for each layer after the application of a 10 km low pass filter and 4 km resampling of the ABD grids, after being converted to density contrasts relative to a background density of 2.7 g cm^{-3}. The gravity response for each layer was determined by first calculating the negative gravity response of the rock slab from the sea surface to the top of the layer followed by calculating the negative gravity response of the rock slab from the sea surface to the bottom of layer using the same 4 km density contrast ABD grid. The difference between these slab responses is the negative gravity surface response of the layer. The negative sign is due to the density contrast being negative relative to 2.70 g cm^{-3} assumed to represent the pre-Zechstein strata. Please note: the background density of 2.70 g cm^{-3} is changed later in equation (5) to 2.60 g cm^{-3}.

The gravity calculation was done in the space domain, using vertical line masses for each of ABD grid nodes, similar to the forward calculations described by Cordell and Henderson (1968). To avoid edge effects the density contrast ABD grids were expanded by 5% (~20 km) using the linear roll off method. The increase in the cell size of the gravity response grids from 100 to 4000 m, was due to the low ~10 km resolution (or ~5 km half wavelength) of the FAA gravity anomaly grid. Correction gravity grids should ideally have the same resolution but not a higher resolution than the FAA gravity grid that is being interpreted, otherwise the interpretation of the final gravity grid could be erroneous.

Determinations of the layer stripped Bouguer anomaly and the sub-Zechstein residual crustal gravity field

To isolate the gravity response of the pre base Zechstein geology, assuming a background density of 2.60 g cc^{-1}, the gravity responses of the sea water layer and the 4 layers down to the base Zechstein (Fig. 17) need to be removed from the FAA (equation 5).

$$\begin{aligned}\text{layer stripped Bouguer anomaly} = \text{FAA} - &(\text{sum of the gravity responses of sea water layerand the 4 layers using negative density contrasts relative to 2.70 g cm}^{-3}) + (\text{sum of the gravity responses of sea water layer and the 4 layers using density of } -0.10\,\text{g cm}^{-3}).\end{aligned} \quad (5)$$

The last term in equation (5) adjusts the stripped Bouguer anomaly such that the reference density for the sub-Zechstein is 2.6 g cm^{-3}. This gives a coherent anomaly pattern – more suited to geological interpretation (Rose 2022).

The density of 2.6 g cm^{-3} is a reasonable value for the Carboniferous even though the Carboniferous densities vary from ~2.7 g cm^{-3} for limestones often forming on the shelf areas around the edge of the basin down to ~2.5 g cm^{-3} for to the Westphalian and Namurian sequences within the basin (Fig. 11).

For completeness, a correction for the topography of the crust/mantle density interface, the gravity effect of the Mohorovičić Discontinuity (Moho), has been applied to the layer stripped Bouguer anomaly (Fig. 18). This correction, called here the isostatic gravity correction, removes the positive gravity effect of the elevated high density upper mantle that exists beneath the crust of the central North Sea basin. The Moho has a 'normal' depth of about 30 to 32 km over much of the onshore UK and decreases to 20 and 25 km beneath the Central Graben of the North Sea (Gatliff *et al.* 1994).

$$\begin{aligned}&\text{sub-Zechstein residual crustal gravity field}\\ &= \text{layer stripped Bouguer anomaly} - \text{isostatic gravity correction}\end{aligned} \quad (6)$$

The isostatic gravity correction grid (Fig. 19a) was derived from the smooth global Moho model (CRUST-1 model after Laske *et al.* 2013) with the lower crust–mantle having an assumed positive density contrast of +0.4 g cm^{-3} relative to the lower crust. Other density contrasts between 0.5 and 0.3 g cm^{-3} were tested but the 0.4 g cm^{-3} best removed the eastward positive trend in the layer

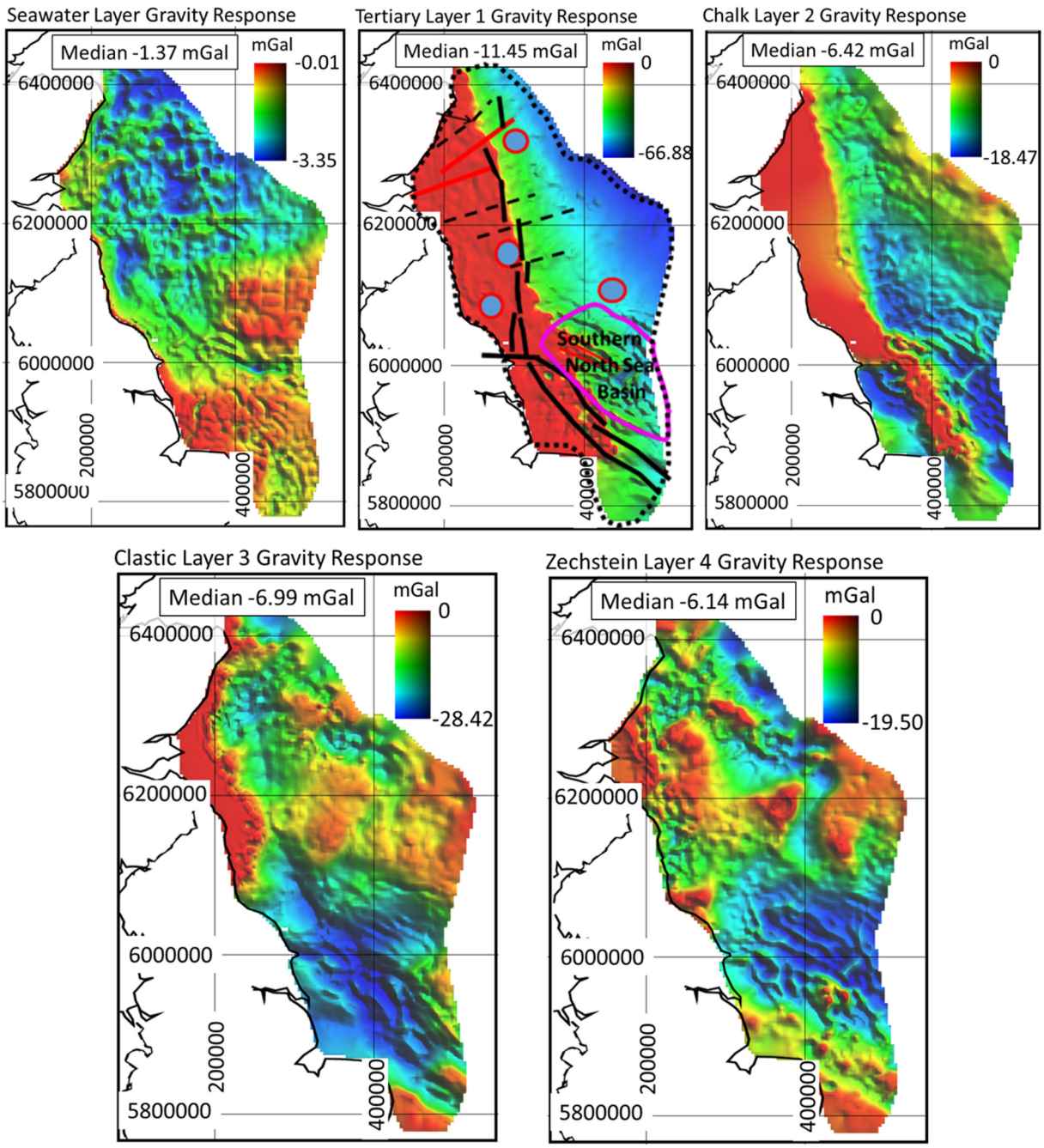

Fig. 17. 4 km grid images of the surface gravity response for each layer, derived from 10 km low pass ABD grids (Fig. 6) using density contrasts relative to a background density of 2.70 g cm^{-3} (changed in equation (5) to 2.60 g cm^{-3}). To relate the interpretation structures (shown in Fig. 1) to the gravity response maps, they have been superimposed on the Tertiary Layer 1 gravity response map.

stripped Bouguer anomaly. Since the Isostatic gravity correction is a long wavelength correction it has little to no effect on the small/intermediate scale gravity anomaly structures but enhances the visualization of the sub-Zechstein residual crustal gravity field such as the Carboniferous basin in the SNS (Fig. 19b).

Regional interpretations of the sub-Zechstein crustal gravity field

The geological and structural interpretations of the sub-Zechstein residual crustal gravity field have inherent uncertainties due to the potential simplicity of the assumption used in generating the gravity responses of the 4 stratigraphic layers, resulting from the regional complexity of the geology making up the layers and underlying basement. The assumption is that a single Gardner's function fits the data for each layer. Inspection of the density–velocity plots (Figs 13–16) clearly show that a relation does exist for each layer but it is noisy and has artifacts. For the Tertiary and Chalk layers 1 & 2, some young formations appear to have been under-compacted, due to the trapping and retention of fluids, giving low density and velocity relationships. Over-compacted strata can also occur in areas where uplift and erosion has removed some of the cover sequences such that the rocks that remain have velocities that would, in normally compacted rocks, be characteristic of greater depth of burial. For the Zechstein layer, Kimbell and Williamson (2015) used well log data to construct a cross plot of layer thickness v. average density and broadly found there is an inverse relationship i.e. it is not devoid of error. This inverse relationship has been used by them to derive the density variation within this layer. In our study, we have used the seismic reflection data (Fig. 2a) to determine an AIV grid

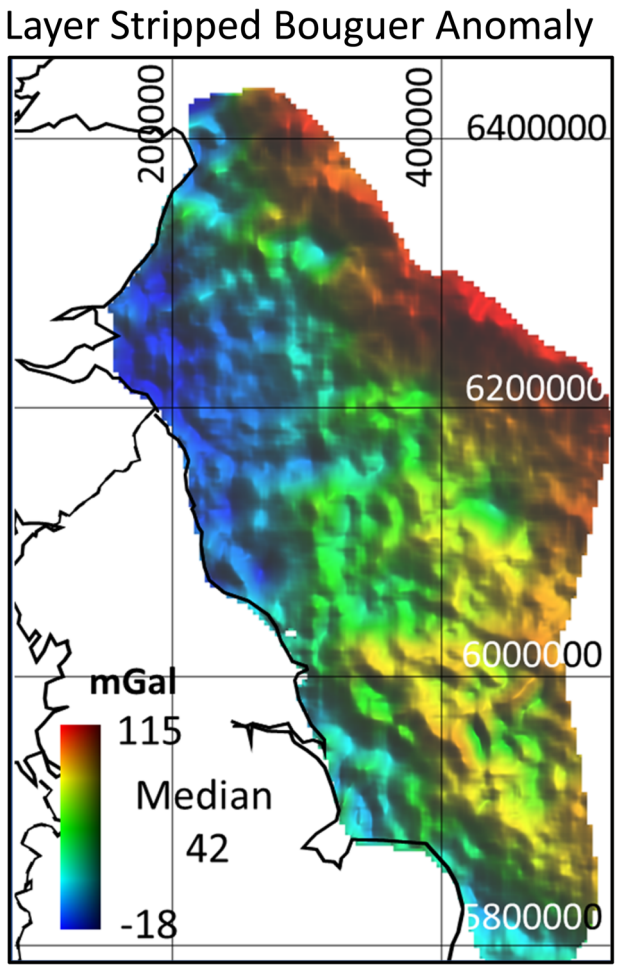

Fig. 18. Layer stripped Bouguer anomaly after gravity layer stripping and assuming background upper crust density of 2.60 g cm^{-3}.

for the Zechstein layer 4, which when coupled with the layer's Gardner's function, using well velocity and density logs, has been used to derive the ABD grid for layer 4 (Fig. 8). How the final density results vary between these two approaches is uncertain, so our interpretation is presently restricted to being qualitative.

Post-Carboniferous subsidence and deformation of the stratigraphic layers

The stratigraphic depth and thickness maps for the 4 layers (Figs 6, 7) clearly show the SNS Basin is a subsiding basin from the Permian into the Tertiary, with strong NNW–SSE to NW–SE structural trends seen in all layer interfaces within the basin, excluding the sea bed. On closer inspection of 2D seismic reflection profile data (Fig. 20) and the stratigraphic surfaces of the top and base Zechstein (Fig. 19), the structural trends are mainly the result of folding rather than from faulting. However, for the base Zechstein (layer 4) there is a significant amount of faulting (Figs 18b, 19). This faulting can be clearly recognized in Figure 21b by the short wavelength nature of the 2D NW–SE lineaments, whereas the 2D NW–SE trending folds are associated with longer wavelength and smoother features as seen for the top Zechstein surface in Figure 21a.

Besides the many geomorphological features seen on the stratigraphic layer surfaces (Fig. 21), fault features cutting the top Zechstein surface (white arrows in Fig. 21a), as defined by their short wavelength, bound the SNS basin to its NE, NW and west sides. The west bounding faults appearing more like a fault zone coinciding with the Dowsing Fault zone to the south of Flamborough Head, truncating the west–east Flamborough fracture zone and continue north of the Flamborough Head as the Central fracture zone (Figs. 1 and 22). The intensity of faulting within the Central fracture zone, however, appears to decrease northwards ending in NW–SE trending en-echelon faults. This suggests the fault zone is transtensional in nature with opening in a NW–SE direction.

Within the centre of the SNS basin, a short SW–NE trending rectangular deep trough feature is identified in the top Zechstein surface and is identified by an oval and '?' in Figure 21a. This feature is a narrow and deep synclinal feature seen in all layer surfaces (Fig. 23). Importantly, the thickness of the Tertiary layer has significantly increased, whereas the thickness of the chalk and clastic layers have remained fairly constant while the thickness of the Zechstein salt layer has significantly decreased. No obvious faults

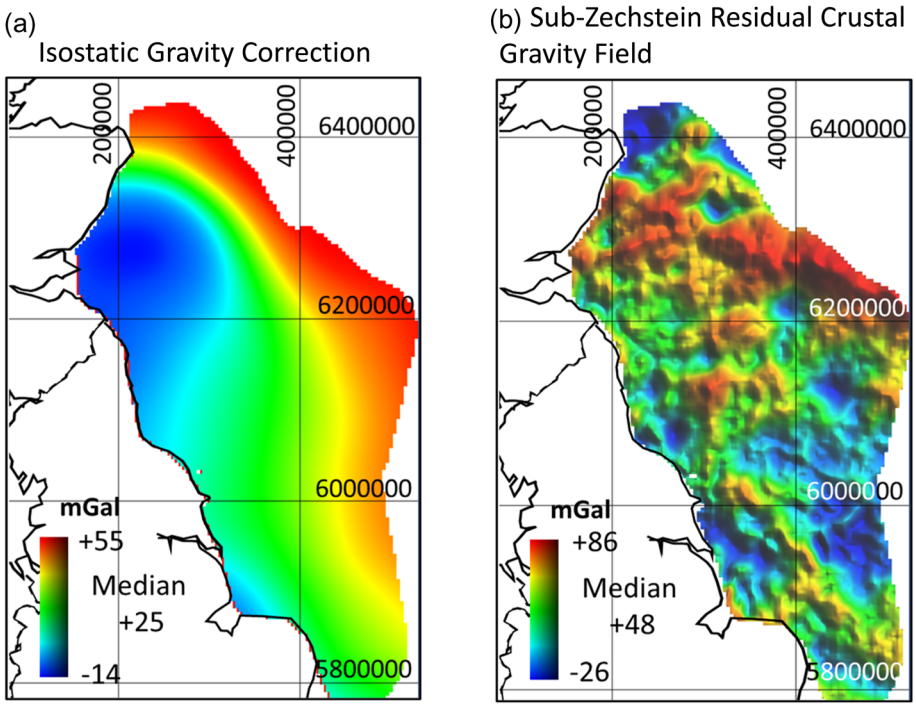

Fig. 19. (**a**) Isostatic correction based on 10 km grid of the CRUST-1.0 model, after Laske *et al.* (2013), (**b**) sub-Zechstein residual crustal gravity field based on equation (6). This image better highlights, in blue, the areas of thick lower density (<2.60 g cc^{-1}) pre-Zechstein strata in the SNS.

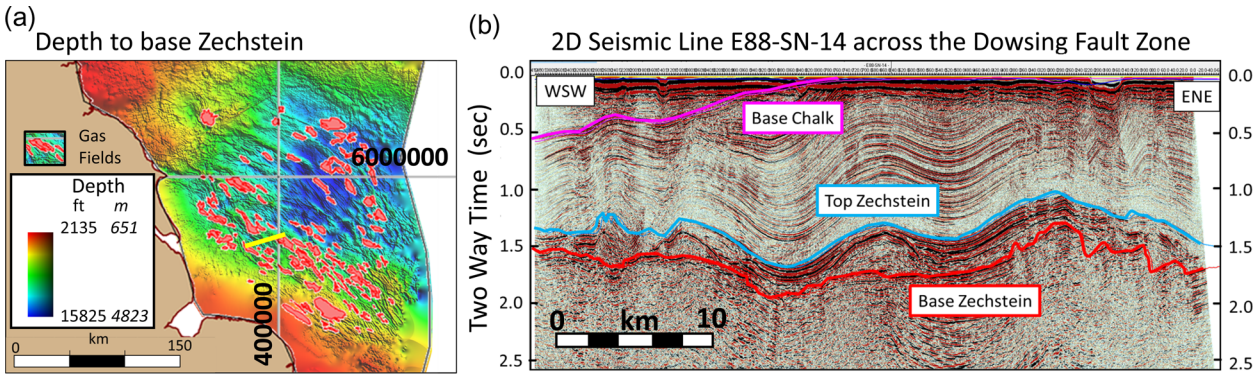

Fig. 20. (**a**) Depth map to base-Zechstein (see Fig. 6) showing the deepest area of subsidence in blue. Overlays on this map are the spatial locations of gas fields (red) and the location of seismic line E88-SN-14 (thick yellow line), (**b**) seismic line E88-SN-14 crossing the Sole Pit inversion high and showing the folding resulting from tectonic movements and halokinesis.

with a SW–NE orientation are seen at the base Zechstein level. After gravity stripping, this feature is seen as a positive anomaly (Fig. 19b). This feature is considered to be an artefact of the gravity stripping method rather than due to any high-density structure in the sub-Zechstein geology. Well log data (44/27-2) only partially samples the feature (Fig. 23) and does not prevent systematic errors being made in the estimate of the bulk densities and derived gravity responses of the sediments within this synclinal feature. However, the geological cause of the feature is fairly clear and is considered to be an overburden response due to the transtensional movements in the overburden along NW–SE faults associated with the salt ridges. The very thin Zechstein layer is likely to be due to salt withdraw on all sides, during the Tertiary, resulting in the subsidence of layers 1, 2 & 3 (Figs 6, 23) and in the increase of Tertiary sedimentation to infill the syncline (Zhang 2020).

The W, NW and NE sides of the SNS basin are marked by fault systems clearly visible in Figure 21a (white arrows) trending SE–NW, SW–NE and WNW–ESE. These faults manifest themselves as tears of Cimmerian age where the subsidence in the centre of the basin has pulled the competent Bacton (lower Triassic) formation into the basin and it has rifted.

The Mid North Sea High

To interpret the sub-Zechstein residual crustal gravity field over the UK sector of the North Sea, the area has been split into two parts, the northern part is named the Mid North Sea High (MNSH) and the southern part is named the Southern North Sea (SNS) Basin. In geological terms, the MNSH gets its name by its position, separating the Northern and Southern Permian basins, and the SNS basin is the north westerly part of the Southern Permian basin (Grant *et al.* 2019).

Previous gravity and magnetic interpretations of the MNSH have been made by the BGS (Kimbell and Williamson 2015; Monaghan *et al.* 2017). The main structures identified are the location of Caledonian granites for both the onshore and offshore, all of which

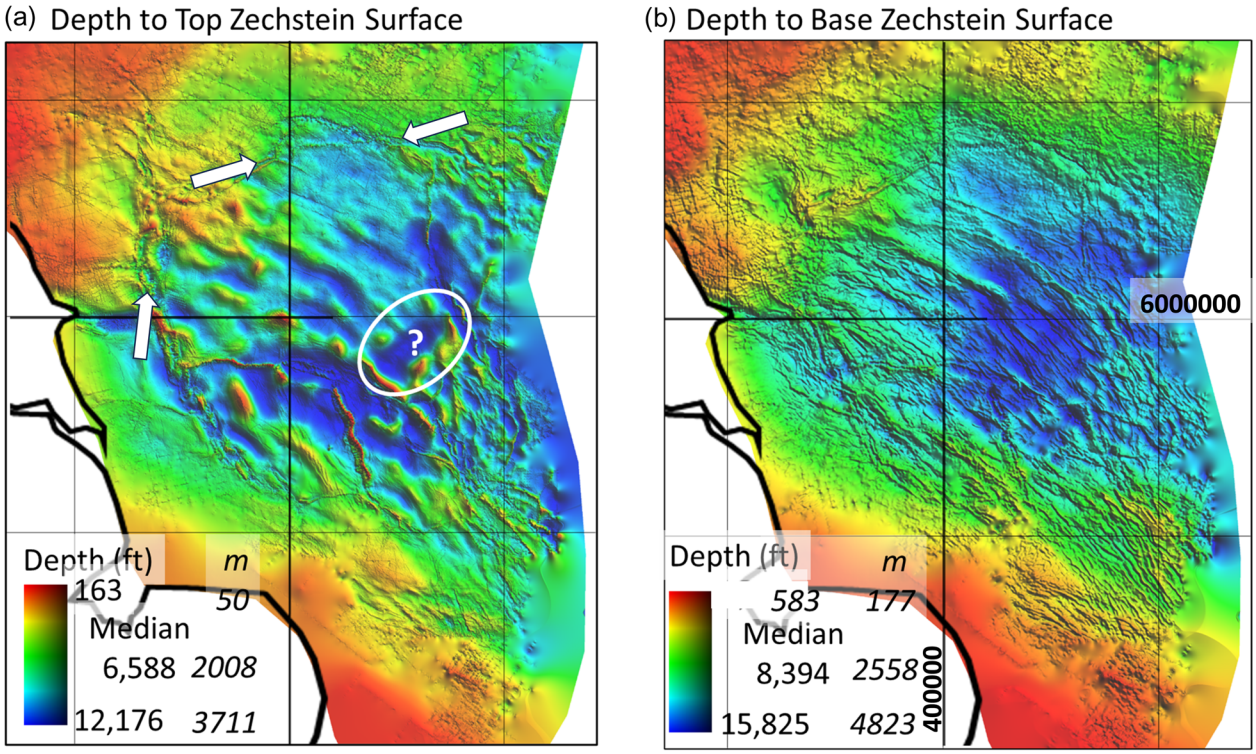

Fig. 21. Zoomed in depth surface images derived from grids of 100 m cell size (Fig. 6) of (**a**) top Zechstein (or base layer 3) showing anomalous SW–NE feature outlined by white oval with '?' and the white arrows identify a fault system trending SE–NW, SW–NE and WNW–ESE, (**b**) base Zechstein (base layer 4).

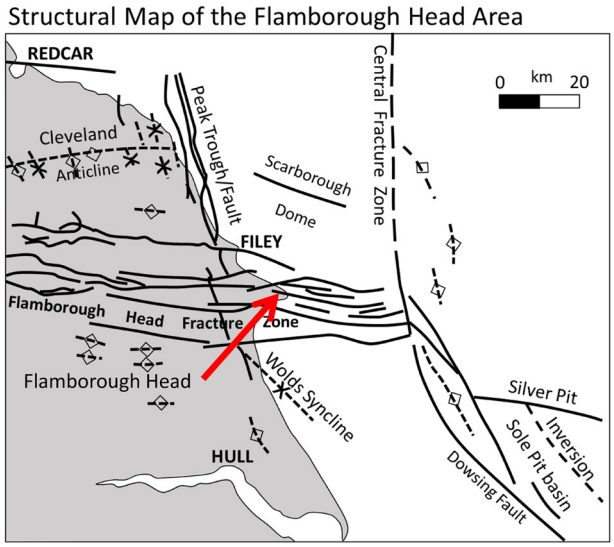

Fig. 22. Regional Structural map of the onshore and offshore Flamborough Head area (redrawn from Roberts *et al.* 2020). For location of the map see Figure 1.

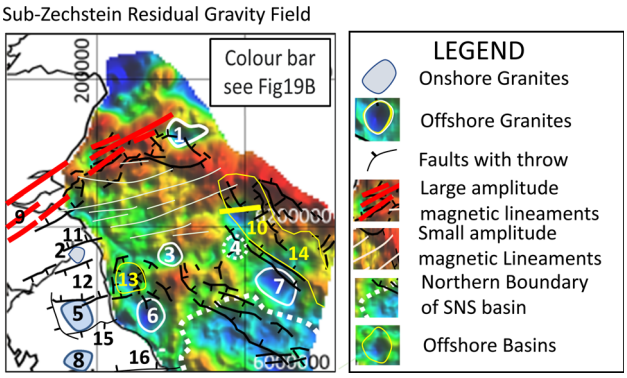

Fig. 24. Existing structural interpretations of the MNSH region based on studies by Kimbell and Williamson (2015) and Monaghan *et al.* (2017), all superimposed on the sub-Zechstein residual crustal gravity field map generated in our study (Fig. 19b). GRANITES: (1) Devil's Hole, (2) Cheviot, (3) Farne – *speculative since seismic data indicates thick Carboniferous sediments*, (4) *Speculative*, (5) North Pennine, (6) Teesside, (7) North Dogger, (8) Wensleydale; BASINS: (9) Midland Valley of Scotland, (10) Quadrant 29 basin, (11) Tweed basin, (12) Northumberland Trough, (13) possible eastward extension of 12, (14) North Dogger basin, (15) Stainmore Trough, (16) Cleveland basin. Location of seismic line in Quadrant 29 (Fig. 25) shown as thick yellow line.

are associated with circular negative gravity anomalies (Fig. 24). For the offshore these anomalies are seen on the BGS Bouguer anomaly map (Figs 4, 5 of Kimbell and Williamson 2015) and on the sub-Zechstein gravity field map (Figs 19b, 24 and 26c). They also calculated a residual Bouguer gravity anomaly, by removal of a 10 km upward continuation field. This revealed a strong offshore WSW–ENE trending grain similar in trend and wavelength to the basin and uplift blocks seen onshore (Fig. 5 of Kimbell and Williamson 2015 and Fig. 24 of this study). It has long been recognized that the Carboniferous basins of NE England are separated by relatively uplifted blocks (Bott and Johnson 1967). This grain is considered to be inherited from the underlying basement and developed during the continental convergence in the Lower Paleozoic by the closure of the Iapetus and Tornquist oceans and subsequent Acadian deformation (Chadwick and Holliday 1991).

A similar trend is also seen as low amplitude magnetic lineaments in the offshore marine magnetic survey (see Figs 6, 7 of Kimbell and Williamson 2015). These lineaments probably represent older structures at depth, located within the crystalline basement. To the north, short-wavelength and high amplitude lineaments (red in Fig. 24) have SW–NE trends extend from the Midland Valley of Scotland to the offshore and are considered to be due to Devonian and Carboniferous magmatism and dyke intrusions.

In this study, we re-evaluate the BGS interpretation of the MNSH gravity data using the gravity layer stripped sub-Zechstein residual crustal gravity field map. Our study supports their findings that are summarized in Figure 23. More recent OGA seismic lines (Fig. 25) also supports the existence of a possible Carboniferous basin in Quadrant 29.

Up until about 2010, potential field studies tended to use the amplitude component of potential field data to interpret the sub-surface geology. With the introduction of the tilt derivative (i.e. the local phase angle of the anomaly signal), this allowed a new way of analysing and interpreting potential field data (Verduzco *et al.* 2004; Fairhead 2015). When the tilt method is applied to the sub-Zechstein gravity field, the tilt derivative is able to identify subtle structural features not immediately obvious in the sub-Zechstein gravity Field. This is illustrated in Figure 26, where the sub-Zechstein residual crustal gravity field (amplitude anomaly) (Fig. 26a) is compared to the tilt derivative (phase angle, Fig. 26b) and the qualitative interpretation based on the tilt derivative (pastel colours, Fig. 26c). The tilt derivative still identifies the granite anomalies but also sharpens up the

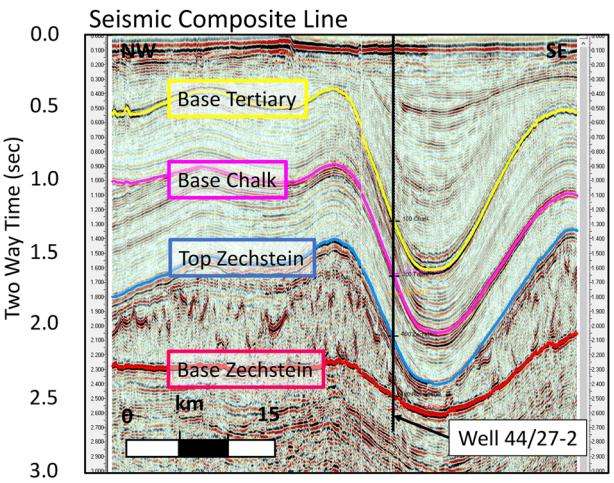

Fig. 23. NW–SE composite seismic profile from 3 surveys crossing the '?' feature shown on the top Zechstein surface in Figure 21a.

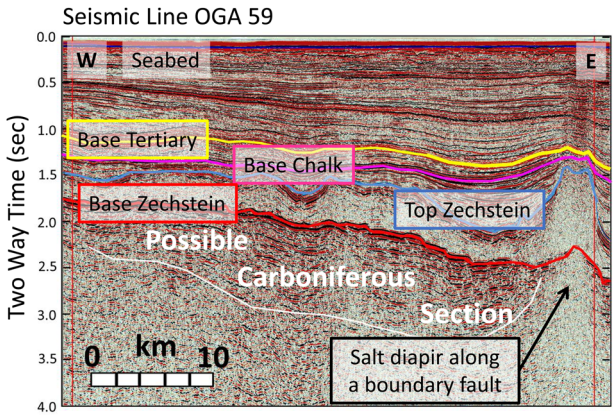

Fig. 25. Seismic 2D profile OGA59. Location shown by thick yellow line in Figure 24 cutting the Quadrant 29 basin.

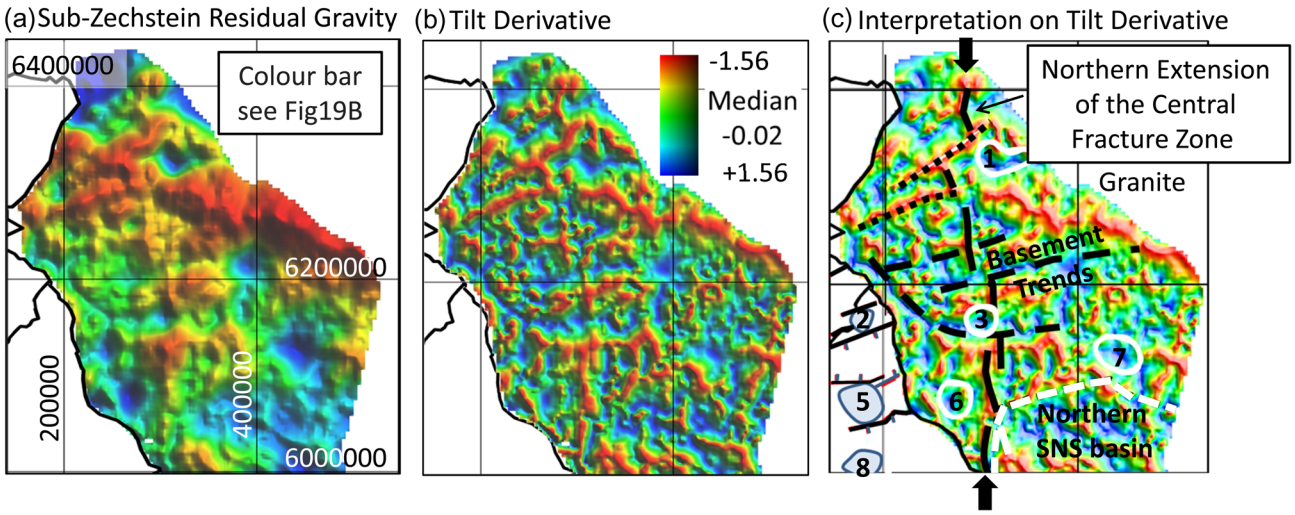

Fig. 26. Mid North Sea High region of North Sea. (**a**) Sub-Zechstein residual crustal gravity field, (**b**) tilt derivative, (**c**) qualitative structural interpretation superimposed on pastel version of the tilt derivative. The SW-NE black dotted lines are magmatic intrusions, the white circles offshore delineate granites (see Fig. 24 caption for names), the WSW–ENE dashed black lines are basement trends similar to structural trends onshore and the south–north thick black offset line interpreted here as a northerly structural continuation of the central fracture zone and Dowsing Fault. To the south (see Fig. 22). the short dashed white line approximately outlines the northern limits of the Southern North Sea Basin.

anomaly and re-enforces the WSW–ENE basement trends (thick dashed lines).

A new, previously unrecognized, south–north positive tilt derivative-based gravity anomaly (solid black offset line in Fig. 26c) extending from the eastern termination of the Flamborough Head fracture zone, north through block 42. Farther north, this south–north gravity anomaly crosses the MNSH and is associated with small offsets by some of the WSW–ENE basement trends (Figs 26c). To the south of the Flamborough Head, the positive tilt gravity anomaly appears to smoothly link with the north–south trending Dowsing fault zone (Fig. 22).

This north–south positive tilt derivative gravity anomaly, north of the Flamborough Head, has been identified from seismic data and is referred to as the Central fracture zone by Grant *et al.* (2019) and Roberts *et al.* (2020). The fracture zone is seismically imaged in Figure 27 and tracked north using the top Zechstein surface which as shown in Figure 27 to have the greatest expression in 2D. Using the regional seismic data shown in Figure 2a to map the layer depth surfaces (Fig. 6), we can only trace the fracture zone to about northing 615 000, north of which the seismic profile track density is too sparse. The correlation of this Central Fracture zone with the positive gravity lineament is extremely good (Fig. 27). In Grant

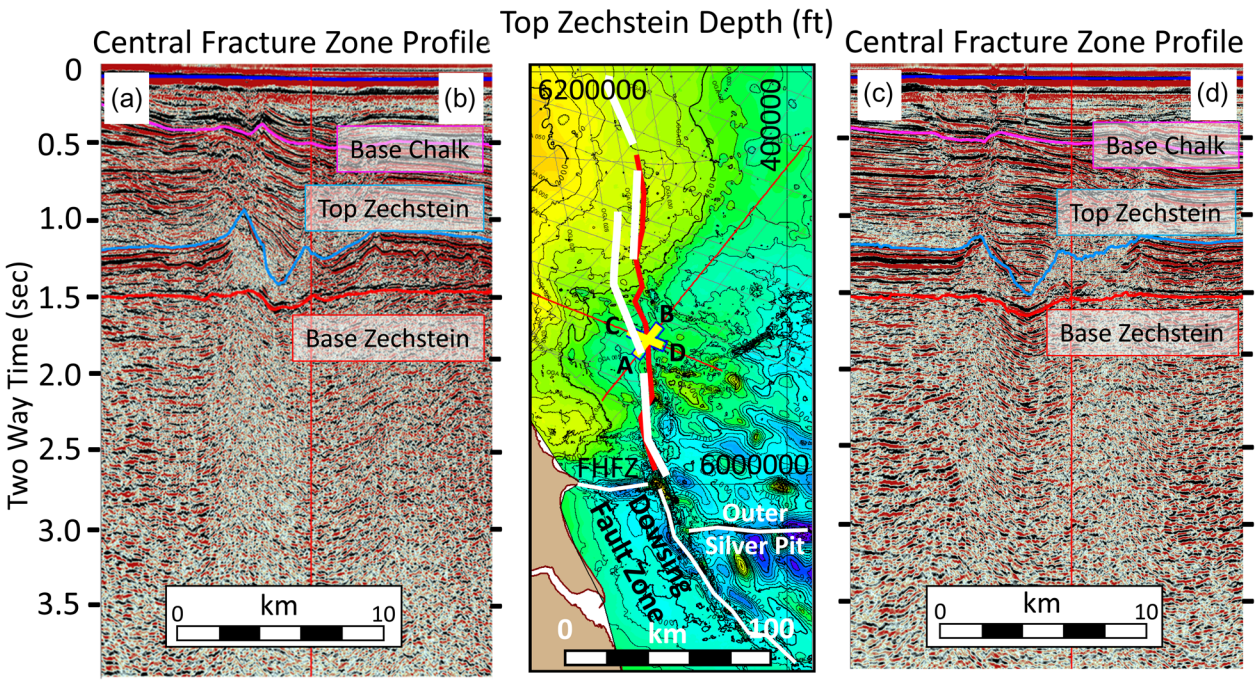

Fig. 27. The central map is the contoured version of the top Zechstein surface showing the locations of the central fracture zone (red line) which extends north of the FHFZ to about northing 6 150 000, the north–south axis of the positive tilt derivative (thick white line) and the two orthogonal seismic profiles (yellow cross) astride the central fracture zone. On either side of the central map are these seismic sections. FHFZ is the Flamborough Head fracture zone (Fig. 22).

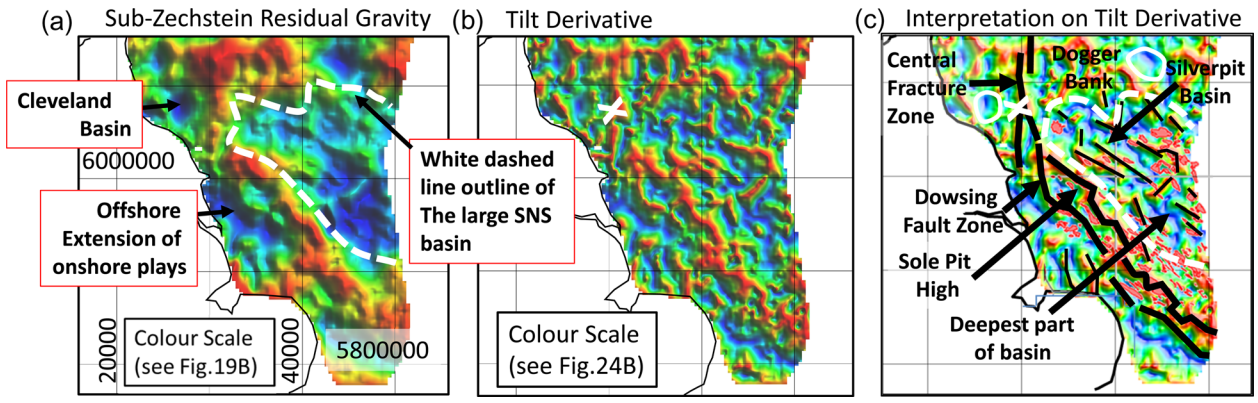

Fig. 28. (**a**) Sub-Zechstein residual crustal gravity field for the Southern North Sea (SNS), (**b**) tilt derivative of the sub-Zechstein residual crustal gravity field. The white 'X' is location of seismic lines shown in Figure 27, (**c**) structural interpretation with locations of the granites (white circles), the outline of the SNS basin (dashed white line), the Dowsing fault zone/Sole Pit inversion structures linking to the south–north central fracture zone (thick black lines) and other faults (thin black lines) seen in the Silverpit basin and deeper parts of the Carboniferous basin. Gas fields are shown in red.

et al. (2019), they show the Central Fracture Zone in a similar way to that shown by Roberts *et al.* (2020), however later in another map they show the Central Fracture Zone is limited to the Dogger Bank. In our study, and based on our satellite gravity data, the fracture zone can be traced north across the Mid North Sea High as a positive linear set of sub-Zechstein residual crustal gravity field and tilt derivative anomalies (Figs 26, 27). Throughout its length, there are small offsets coinciding with the WSW–ENE basement trends that have controlled the faulting and basin development onshore (Fig. 26c). Inspection of the BGS marine, reduced to pole (RTP), magnetic anomaly map (Fig. 7 of Kimbell and Williamson 2015) indicates no magnetic anomalies are associated with the Central fracture zone, so it is not a structure associated with higher susceptibility. The only correlation seen in our study is that it has a similar south–north trend as seen in Figures 6–8, east of which all layers 1 to 4 thicken. Could this be a basement fault-controlled hinge zone? Pre-Permian imaging of the seismic data is too poor to answer this question.

The Southern North Sea Basin

The quantitative interpretation of the SNS Basin area is shown superimposed on a pastel shaded version of the tilt derivative anomaly map (Fig. 28c). As with the MNSH (Fig. 26), the clean image versions of both the sub-Zechstein residual crustal gravity field and tilt derivative maps, are shown, so that one can see the evidence for the quantitative interpretation. With the geological noise imbedded within the data processing noise, one has to guard against over interpretation of the gravity data.

Geology studies of the SNS Basin reveal a complex history of subsidence that occurred in the Paleozoic, Mesozoic, and Cenozoic (Glennie and Underhill 1998; Balson *et al.* 2001) causing subsidence in the stratigraphic layer interfaces (Fig. 6). Rifting and crustal extension of the basin occurred in the late Paleozoic and early Mesozoic. These tectonic events which commenced in the late Carboniferous caused folding, faulting, uplift and inversion of the Carboniferous rocks as well as halokinesis. A strong influence of NW–SE tectonic trends and strike-slip reactivation of basement faults occurred with this inversion. Further uplift occurred in the Mesozoic followed by a major phase of basin inversion during the Cenozoic. This inversion reactivated pre-existing faults which allowed the salt tectonics to remain active into the Tertiary (Glennie 1986; Cameron *et al.* 1993).

The SNS basin is the largest gas producing basin in the UK continental shelf, with gas sourced from the Carboniferous Westphalian and Namurian strata (Coal Measures) migrating into the lower Permian sandstones reservoirs, where it is sealed by the upper Permian Zechstein salt. Since the Westphalian strata is low density (density <2.60 g cm^{-3}, Fig. 11), it shows up in Figure 28a as a negative gravity anomaly with its maximum thickness coinciding with the largest negative anomaly. Within the basin, NW–SE faults bounding the Silverpit basin are imaged in Figure 28c and are pre-Permian in origin (Grant *et al.* 2019). The approximate northern limit of the basin is delineated by the dashed white line in Figure 28a, c where Carboniferous shelf limestones and shallow basement have densities >2.60 g cm^{-3} and generate positive anomalies in Figure 28a. This northern boundary of the SNS basin is also supported by the northern limits of the NW–SE faulting and folding of the base Zechstein surface and the faulting associated with the Bacton (lower Triassic) formation (Fig. 21 & section post-Carboniferous subsidence and deformation of the stratigraphic layers). The eastern and SE limits of the basin are truncated by the UK median line but continue into the Netherlands North Sea area.

To the west and SW, the basin is bounded by a WNW–ESE trending broad positive isostatic anomaly (Fig. 28a). This anomaly is part of the Sole Pit High which formed as a result of basin inversion and basement uplift and represents a complex network of transpressional and transtensional faults of Permian Rotliegend age. These fault structures are thought to represent the upward termination of a series of wrench-induced flower structures with a right-lateral sense of displacement (Grant *et al.* 2019). The Sole Pit High is bounded on its SW side by the Dowsing Fault zone (Fig. 28c) and has a northern continuation as the central fracture zone (see the Mid North Sea High section).

Conclusions

The strategy and aim of this gravity layer stripping study, has been to isolate, image and geologically interpret the gravity response of the sub-Zechstein geology beneath the UK sector of the North Sea. This has been achieved by the initial removal of the sum effect of the gravity responses of the sea water, the 4 stratigraphic layers and the Moho topography from the FAA gravity data. For the 4 stratigraphic layers this involved determining representative Gardner's velocity-density functions, so that the average interval velocity (AIV) grids could be converted to average bulk density (ABD) grids, from which the gravity response grids of each layer could be determined. This method is considered more constrained and accurate than just using an interpolation and extrapolation polynomial function in areas of poorly distributed well density log data, such as the northern half of the study area. Gardner's velocity–density function for each layer covering the whole of the UK sector of the North Sea is questionable in its accuracy due to local and regional changes in stratigraphy. This problem is clearly seen in the cloud nature of the functions when all

well data are used. To improve the determination of the Gardner's velocity–density function, two stages of filtering/resampling were applied in part to reduce the overall number of data points and in part to reduce the biasing of the data for heavily sampled depth sections. This filtering/resampling has significantly improved the definition of the function and lessens the biasing effects of anomalous zones of under- or over-compaction.

The resulting sub-Zechstein residual crustal gravity field reveals that all the gravity anomalies and structures previously identified by BGS studies are seen in this study to indicate the methodology used has some merits and is able to identify additional anomalies and structures. In conclusion, the study

- Clearly shows that the layer depth maps identify the spatial extent of subsidence defining the SNS basin from the Permian into the Tertiary. The layer depth maps also define the spatial extent and nature of the tectonic deformation, in the form of folding and faulting, that has taken place within the interior of the SNS basin.
- Identifies, the size and spatial extent of the negative sub-Zechstein residual crustal gravity field anomaly associated with the SNS basin which helps to define the spatial extent of the low-density Carboniferous Westphalian and Namurian strata within the basin. This spatial extent is similar in area to that affected by the layer depth subsidence.
- Identifies NW–SE trending gravity anomalies, associated with faulting within the SNS basin, which define the Sole Pit and Silver Pit basins.
- Identifies a broad NNW–SSE trending positive gravity anomaly that bounds the SNS basin on its western side and coincides with the Sole Pit basement high and the Dowsing fault zone.
- Identifies for the first time the basin boundary faults, on the W, NE and NW sides of the basin, associated with the Bacton (lower Triassic) formation.
- Identifies for the first time a linear offsetting positive gravity lineament on both the sub-Zechstein residual crustal gravity field and tilt anomaly maps extending north from the eastern termination of the Flamborough Head fracture zone. This gravity lineament appears to form the northern continuation of the Dowsing Fault zone. North of the Flamborough Head fracture zone, the gravity lineament closely parallels the Central fracture zone which can be traced as far north as northing 6 150 000. Farther north, the gravity lineament crosses the MNSH and has offsets that coincide with WSW–ENE basement trends. This suggests the gravitational source structure of the lineament lies within the basement or its topology. The gravity lineament also parallels the north–south boundary (hinge zone) where the North Sea sediments thicken to the east suggesting it relates to a basement structure (Figs 6, 7).

Despite the potential limitations that the gravity stripping method may have when considering large study areas, this study has shown it to be an effective tool in the investigation of deep structures within sedimental basins and underlying basement of the UK sector of the North Sea.

Acknowledgements To Getech Group plc for the use of their grid based potential field processing and imaging software 'GETgrid'. Many thanks to Xinhe Zhang for his contribution to this work during his MSc project. Thanks also goes to Christian Olaf Mueller and an anonymous reviewer for their input that has improved the text and lastly to Lucy Bell (*Petroleum Geoscience*) for her help and guidance.

Author contributions **JDF**: conceptualization (equal), supervision (equal), writing – original draft (lead); **DM**: conceptualization (equal), formal analysis (equal), supervision (equal); **NMA**: formal analysis (equal); **İÖ**: formal analysis (equal); **DM**: formal analysis (equal); **OR**: formal analysis (equal); **CMG**: project administration (lead), resources (lead), supervision (equal)

Funding This research received no specific grant from any funding agency in the public, commercial, or not-for-profit sectors.

Competing interests The authors declare that they have no known competing financial interests or personal relationships that could have appeared to influence the work reported in this paper.

Data availability The datasets generated during and/or analysed during the current study are available in their original form Bathymetry from 2016 version of the EMODnet DTM (https://emodnet.ec.europa.eu) and all other data from the North Sea Transition Authority.

References

Azli, N.M. 2018. *Resolution Analysis of Satellite Gravity Data for Exploration Prospect Analysis: Mid-North Sea High and Southern North Sea*. MSc Dissertation, University of Leeds, 64.

Balson, P., Butcher, A., Holmes, R., Johnson, H., Lewis, M. and Musson, R. 2001. *North Sea Geology*. British Geological Survey, Technical Report **TR_008**, 1–48.

Bott, M.H.P. and Johnson, G.A.L. 1967. The controlling mechanism of carboniferous cyclic sedimentation. *Journal of the Geological Society*, **123**, 421–444.

Brocher, T.M. 2005. *Compressional and Shear Wave Velocity Versus Depth in the San Francisco Bay Area, California: Rules for USGS Bay Area Velocity Model 05.0.0 U.S.* Geological Survey, Open-File Report **2005-1317 Version 1.0**.

Cameron, D., van Doorn, D., Laban, C. and Streif, H.J. 1993. Geology of the Southern North Sea basin. Proceedings 8th Sympoium on Coastal and Ocean Management, New Orleans, 14–26.

Chadwick, R.A. and Holliday, D.W. 1991. Deep crustal structure and Carboniferous basin development within the Iapetus convergence zone, northern England. *Journal of the Geological Society*, **148**, 41–53, https://doi.org/10.1144/gsjgs.148.1.0041

Christensen, N. and Mooney, W. 1995. Seismic velocity structure and composition of the continental crust: a global view. *Journal of Geophysical Research: Solid Earth*, **100**, 9761–9788, https://doi.org/10.1029/95JB00259

Cordell, L. and Henderson, R.G. 1968. Iterative three-dimensional solution of gravity anomaly data using a digital computer. *Geophysics*, **33**, 596–601, https://doi.org/10.1190/1.1439955

EDCON-PRJ 2015. *Mid-North Sea High Offshore East United Kingdom 2-D Marine Gravity and Magnetic Survey Final Processing Report*. EDCON-PRJ, Inc.

Fairhead, J.D. 2015. *Advances in Gravity and Magnetic Processing and Interpretation*. EAGE Publications bv.

Filina, I., Delebo, N. *et al.* 2014. Gravity modeling in the western Gulf of Mexico to support seismic imaging. SEG, 84th Ann. Int meetng Denver USA, Expanded Abstracts, 1264–1268.

Gardner, G.H.F., Gardner, L.W. and Gregory, A.R. 1974. Formation velocity and density the diagnostic basis for stratigraphic traps. *Geophysics*, **39**, 2085–2095, https://doi.org/10.1190/1.1440465

Gatliff, R.W., Richards, P.C. *et al.* 1994. *United Kingdom Offshore Regional Report: The Geology of the Central North Sea*. HMSO for the British Geological Survey, London.

Glennie, K. 1986. Development of NW Europe's Southern Permian gas basin. *Geological Society, London, Special Publications*, **23**, 3–22, https://doi.org/10.1144/GSL.SP.1986.023.01.01

Glennie, K. and Underhill, J. 1998. Origin, development and evolution of structural styles. *In:*Glennie, K.W. (ed.) *Petroleum Geology of the North Sea: Basic Concepts and Recent Advances*. Wiley, Hoboken, NJ, 4th edn. Chapter 2, 42–84, https://doi.org/10.1002/9781444313413.ch2

Grant, R.J., Underhill, J.R., Hernandez-Casado, J., Jamieson, R.J. and Williams, R.M. 2019. The evolution of the dowsing graben system: implications for petroleum prospectivity in the UK Southern North Sea. *Petroleum Geoscience*, **27**, art. no. petgeo2018-064, https://doi.org/10.1144/petgeo2016-021

Green, C.M., Fletcher, K.M.U., Cheyney, S., Dawson, G.J. and Campbell, S.J. 2019. Satellite gravity – enhancements from new satellites and new altimeter technology. *Geophysical Prospecting*, **67**, 1611–1619, https://doi.org/10.1111/1365-2478.12697

Japsen, P. 1998. Regional velocity-depth anomalies, North Sea Chalk: a record of overpressure and neogene uplift and erosion. *AAPG Bulletin*, **82**, 2031–2074.

Japsen, P. 1999. Overpressured Cenozoic shale mapped from velocity anomalies relative to a baseline for marine shale, North Sea. *Petroleum Geoscience*, **5**, 321–336, https://doi.org/10.1144/petgeo.5.4.321

Japsen, P. 2000. Investigation of multi-phase erosion using reconstructed shale trends based on sonic data. Sole Pit axis, North Sea. *Global and Planetary Change*, **24**, 189–210, https://doi.org/10.1016/S0921-8181(00)00008-4

Kimbell, G.S. and Williamson, J.P. 2015. *A Gravity Interpretation of the Central North Sea*. British Geological Survey Commissioned Report **CR/15/119N**, http://nora.nerc.ac.uk/516759/5

Kimbell, G.S., Carruthers, R.M., Walker, A.S.D. and Williamson, J.P. 2006. *Regional Geophysics of Southern Scotland and Northern England. Version 1.0 on CD-ROM*. Nottingham: British Geological Survey, Keyworth.

Laske, G., Masters, G., Ma, Z. and Pasyanos, M. 2013. Update on CRUST1. 0—A 1- degree global model of Earth's crust. *In:* Geophysical Research Abstracts, 2658. EGU General Assembly Vienna, Austria.

Maxwell, D. 2020. *Density Modelling and Gravity Stripping of Sub-Zechstein Geological Structures in the UK Sector of the Southern North Sea*. MSc Dissertation, University of Leeds, 67.

Monaghan, A., Arsenikos, S. *et al.* 2017. Carboniferous petroleum systems around the Mid North Sea High, UK. *Marine and Petroleum Geology*, **88**, 282–302, https://doi.org/10.1016/j.marpetgeo.2017.08.019

Nwozor, K.K., Onuorah, L.O. *et al.* 2017. Calibration of Gardner coefficient for density–velocity relationships of tertiary sediments in Niger Delta Basin. *Journal of Petroleum Exploration and Production Technology*, **7**, 627–635, https://doi.org/10.1007/s13202-017-0313-7

Özsöz, İ. 2019. *Gravity Layer Stripping for Analysis of Jurassic, Triassic and Pre-Zechstein North Sea Units*. MSc Dissertation, University of Leeds, 103.

Quijada, M.F. and Stewart, R.R. 2007. *Density Estimations from Density-Velocity Relation and Seismic Inversion*. CREWES Research Report – Volume **19**.

Roberts, N.M.W., Lee, J.K., Holdsworth, R.E., Christopher Jeans, C., Farrant, A.R. and Haslam, R. 2020. Near-surface Palaeocene fluid flow, mineralisation and faulting at Flamborough Head, UK: new field observations and U-Pb calcite dating constraints. *Solid Earth*, **11**, 1931–1945, https://doi.org/10.5194/se-11-1931-2020

Rose, O. 2022. *Gravity Layer Stripping to Investigate Carboniferous Structures of the Southern North Sea*. MSc Dissertation, University of Leeds, 95.

Sobolev, S. and Babeyko, A.Y. 1994. Modeling of mineralogical composition, density and elastic wave velocities in anhydrous magmatic rocks. *Surveys in Geophysics*, **15**, 515–544, https://doi.org/10.1007/BF00690173

Van Der Molen, A.S. 2004. *Sedimentary Development, Seismic Stratigraphy and Burial Compaction of the Chalk Group in the Netherlands North Sea Area*. Dissertation, UU Department of Earth Sciences, 175.

Verduzco, B., Fairhead, J.D., Green, C.M. and MacKenzie, C. 2004. New Insights into magnetic derivatives for structural imaging. *The Leading Edge*, **23**, 116–119, https://doi.org/10.1190/1.1651454

Zhang, X. 2020. *Zechstein and Post-Zechstein Density Modelling and Gravity Stripping in the Southern North Sea*. MSc Dissertation, University of Leeds, 97.